Emulating the Illustris-TNG simulation with a Semi-analytic model

Osase Omoruyi,[1★] Bryan Terrazas,[2] Yossi Cohen[3] Viraj Pandya[4] Rachel Somerville[5] Lars Hernquist[1]
[1] *Center for Astrophysics | Harvard & Smithsonian, 60 Garden St., Cambridge, MA 02138, USA*
[2] *Department, Institution, Street Address, City Postal Code, Country*
[3] *Another Department, Different Institution, Street Address, City Postal Code, Country*
[4] *Another Department, Different Institution, Street Address, City Postal Code, Country*
[5] *Another Department, Different Institution, Street Address, City Postal Code, Country*

Accepted XXX. Received YYY; in original form ZZZ

ABSTRACT

Semi-analytic models (SAMs) are powerful tools for studying galaxy formation due to their computational efficiency and flexibility. However, they often rely on simplified prescriptions for key physical processes such as gas cooling, star formation, and feedback. Although hydrodynamical simulations also rely on simplified treatments for the physics below their resolution (e.g. star formation), they still offer more detailed modeling of the processes above their resolution. In this work, we leverage the strengths of the flexible Santa Cruz SAM and the detailed IllustrisTNG 100 Mpc hydrodynamic simulation to create the TNG SAM, a SAM calibrated to emulate the underlying flow of baryons in the TNG Universe. To create the TNG SAM, we ran the Santa Cruz SAM on TNG100's dark-matter-only merger trees and focused on reproducing the baryon cycle for galaxies with halo masses $M_{200} < 10^{12} M_{\odot}$, where stellar feedback dominates. The new TNG SAM uses physical insights from TNG to introduce several key updates to the baryon cycle in the SC SAM's galaxy formation framework: 1) a prescription for the efficiency of halo gas (re-)accretion, 2) a revised cooling recipe for gas transitioning from the hot halo to the galaxy based on cooling time, eliminating the traditional "cold mode" vs. "hot mode" dichotomy, 3) the incorporation of both galactic and halo-scale outflows, and 4) metallicity-dependent mass loading factors that describe the circulation of metals between galaxies and their halos. These calibrations not only enable the TNG SAM to reproduce TNG's underlying flow of gas and metals from the scale of the galaxy to the halo, but also global galaxy (e.g., stellar mass) and halo (e.g. baryon fraction) properties within $\sim 30\%$ accuracy up to $z = 6$. This demonstrates that, with proper calibrations, SAMs can effectively capture the complex physics of galaxy formation seen in hydrodynamical simulations. revising

Key words: galaxies: evolution – galaxies: formation – galaxies: halos – methods: numerical

1 INTRODUCTION

Observations across the electromagnetic spectrum have revealed a Universe rich in dark matter, stars, gas, and dust, sparking numerous questions regarding their formation and evolution. The Λ Cold Dark Matter (ΛCDM) model of cosmological structure formation proposes that the Universe consists of a complex filamentary network molded by gravity and populated with dark matter halos . Within these halos, baryonic matter falls to the center of the gravitational potential well, condenses, and forms galaxies (White & Rees 1978). To study this process from cosmological to stellar scales, numerous studies have used numerical simulations to predict and correlate observable galaxy properties– such as stellar mass, cold gas mass, and rate of star formation– with dark matter halo characteristics (see Somerville & Davé (2015) for a comprehensive review). With the advent of powerful observatories like the *JWST* and the upcoming *Nancy Grace Roman Space Telescope*, our ability to observe galaxies in the earliest days of the Universe and across larger cosmic volumes is rapidly improving, necessitating the development of more sophisticated and flexible cosmological models of galaxy formation.

Understanding how galaxies form and evolve requires investigating how they interact with their surrounding environment. As dark matter halos grow, galaxies accrete gas from the intergalactic medium (IGM) into the circumgalactic medium (CGM), connecting the large-scale cosmic web with the galaxies at the centers of these halos. Gravity continues to drive flows of gas from the CGM into the interstellar medium (ISM), fueling star formation. As stars form, evolve, and eventually die, the resulting feedback from stellar winds, supernovae (SNe), and black hole activity heats and/or expels material back into the CGM or IGM. This matter can later be re-accreted, fueling new star formation. This cycle of gas accretion, star formation, feedback, and re-accretion—known as the "baryon cycle"— is fundamental to shaping how galaxies evolve.

To model the baryon cycle within the ΛCDM paradigm, two primary modeling techniques have emerged: numerical hydrodynamical simulations and semi-analytic models (SAMs). Improving upon dark-matter and gravity-only simulations to include baryonic physics, numerical hydrodynamical simulations explicitly solve equations of gravity, (magneto)hydrodynamics, and thermodynamics. This com-

★ E-mail: osase.omoruyi@gmail.com

prehensive approach enables them to self-consistently model the coupled evolution of dark matter, gas, stars, and black holes, providing detailed information on each component's spatial distribution, temperature, and kinematics. However, simulating large cosmological volumes at high resolution presents challenges. To capture the essential physics occurring below their resolution limits, such as star formation and black hole feedback, these simulations rely on phenomenological "subgrid recipes" that contain adjustable parameters calibrated to reproduce a given set of observations. Additionally, the computational expense of hydrodynamical simulations also limits their ability to explore variations in subgrid models across vast volumes.

In contrast, SAMs offer a computationally efficient alternative by treating galaxies as unresolved entities and relying solely on "subgrid" recipes to simulate their formation and evolution. Built from dark matter-only N-body simulations or semi-analytic approaches based on merger trees (e.g., Press-Schechter formalism), SAMs bridge the gap between the hierarchical growth of dark matter halos and observed galaxy populations by employing simplified analytical models of key physical processes relevant to galaxy evolution (White & Frenk 1991; Cole 1991; Lacey & Silk 1991). In a SAM, a galaxy is typically represented as a collection of mass reservoirs, such as the stellar disk, stellar bulge, cold gas disk, hot halo gas, and ejected material. As a result, SAMs essentially function as "flow models," solving ordinary differential equations to track the flow of baryons between each component, with the flows governed by the physical prescriptions included in the model. The specific processes modeled, such as radiative cooling, chemical evolution, and feedback, lie at the discretion of the model's creator. Some SAMs incorporate a wide variety of detailed physical prescriptions (e.g., Santa Cruz Somerville et al. 2008b, SAGE Croton et al. 2006, GALFORM Lacey et al. 2016, SHARK Lagos et al. 2018), while others focus on a more limited set of deemed most critical for galaxy formation (e.g., Davé et al. 2012; Bouché et al. 2010). This flexibility allows SAMs to be tailored to specific scientific questions and computational resources, making them a valuable tool for understanding the "big picture" of the complexities shaping galaxy evolution.

Despite their different approaches, highlighted in Table 1, both SAMs and hydrodynamical simulations share a reliance on phenomenological prescriptions to simulate fundamental processes in the baryon cycle. This has led to the practice of "fine-tuning" or calibrating these models to reproduce a selection of observations, introducing additional uncertainty when comparing and interpreting results. Early comparisons of SAMs and hydrodynamical simulations (e.g. Benson et al. 2001; Helly et al. 2003; Yoshida et al. 2002; Saro et al. 2010; Stringer et al. 2010) found general agreement in predicting properties such as the overall distribution of galaxies and their cold gas mass fractions, but differences properties like the efficiency of gas cooling, star formation histories, and the merger history of specific galaxies. More detailed comparisons (e.g. Stringer et al. 2010; Monaco et al. 2014; Guo et al. 2016; Mitchell et al. 2018; Côté et al. 2018) similarly found that SAMs can approximate key galaxy properties such as stellar mass functions and specific star formation rates to a reasonable degree of accuracy when compared to hydrodynamical simulations. However, they also highlighted significant differences in the treatment of gas cooling, star formation efficiencies, galaxy sizes, and the evolution of star formation rate density. These results suggest that discrepancies between the two methods may arise from specific parameterizations and models used, rather than inherent limitations of each approach.

Recognizing SAMs and hydrodynamical simulations as complementary, rather than competing, techniques, can significantly enhance their predictive power. While SAMs offer computational efficiency through simplified, phenomenological models, they can be significantly improved by incorporating the detailed physical insights provided by hydrodynamical simulations. For instance, Pandya et al. (2020) compared results from the FIRE-2 numerical hydrodynamic simulations (Hopkins et al. 2018) with those of the Santa Cruz SAM (SC SAM) for a suite of halos with masses ranging from 10^{10} – 10^{12} $\mathrm{M}_{\odot}$. They found substantial agreement between FIRE-2 and the SC SAM for stellar and cold gas masses, but significant disagreements in the properties of the hot halo gas — a measurement not widely available for calibrating or validating models, particularly for Milky Way and lower mass halos. By adjusting the SAM to account for the suppression of halo gas accretion via stellar winds, particularly in dwarf galaxies, Pandya et al. (2020) were able to reproduce the reduced halo gas accretion efficiencies of the FIRE-2 complementary galaxies remarkably well. Similarly, Côté et al. (2018) refined GAMMA, a SAM aimed at understanding the chemical evolution of low-mass galaxies and the origins of metal-poor stars, by calibrating it against the observable properties of the most massive galaxy in the Wise et al. (2011) high-redshift hydrodynamical simulation. They found that implementing a non-uniform mixing model was key to reproducing the observable quantities in the hydrodynamical simulation. In an extended exercise to model the role of the CGM and its energy content in governing the evolution of galaxies, Pandya et al. 2023 used the FIRE-2's predictions for the flows of mass and energy in a given set of halos to calibrate their model. This approach enabled them to successfully emulate the detailed baryon cycle modeled in FIRE-2, further demonstrating the effectiveness of this integrated approach. regulator models for galaxy evolution that emphasize the role of the circumgalactic medium (CGM) and its energy content in governing the supply of star-forming gas

In this work, we extend these efforts to devise more realistic subgrid prescriptions for cosmological simulations by comparing the predictions of The Next Generation Illustris simulations (IllustrisTNG) with the Santa Cruz SAM, both of which have demonstrated success in reproducing a wide range of observations. Building on the initial comparisons between the two simulations made by Gabrielpillai et al. (2022), we modify the Santa Cruz SAM's galaxy formation model to better emulate the detailed physical processes observed in the IllustrisTNG simulations, with a specific focus on mirroring TNG's treatment of stellar feedback. By utilizing measurements detailing galaxy- and halo-scale inflow and outflow rates for a subset of TNG100 galaxies (Cohen et al (2024), in prep) and calibrating the SAM to match them, we create a new "TNG SAM," visualized in Figure 2. This endeavor serves three primary goals: (1) to simplify and distill TNG's complex feedback and baryon cycle behaviors into a more interpretable semi-analytic framework, (2) to extend the predictive power of galaxy formation studies beyond the computational limits of hydrodynamical simulations, and (3) to enable direct comparisons between different galaxy formation modeling techniques, highlighting their strengths and weaknesses.

This paper is structured as follows: In Section 2, we describe the IllustrisTNG hydrodynamical simulations and the Santa Cruz SAM, and how we compare the output from both models. In Section 3, we present modifications made to the SC SAM's galaxy formation model that form the basis of the new "TNG SAM." The results of these modifications are presented in Section 4. In Section 5, we examine the factors contributing to the TNG SAM's success, along with its limitations and potential areas for improvement. Finally, 6 provides a concise summary of the key takeaways from this exercise.

2 MODEL DESCRIPTIONS

In this section, we describe the two models used in this study: the IllustrisTNG hydrodynamical simulations and the Santa-Cruz semi-analytic model, with their key parameters summarized in Table 1. We also outline the methods used to compare the outputs of the Santa Cruz SAM with TNG.

2.1 The IllustrisTNG Simulations

The IllustrisTNG simulations (hereafter TNG) are a suite of graveto-magnetohydrodynamical simulations that model the physical processes governing the formation and evolution of galaxies across different cosmological volumes (Springel et al. 2018; Weinberger et al. 2017; Pillepich et al. 2018b; Nelson et al. 2018). The suite includes nine simulations, with box sizes of 50, 100, and 300 Mpc^3, each run at three different resolutions (1 being the highest and 3 the lowest; Marinacci et al. 2018; Naiman et al. 2018; Springel et al. 2018; Nelson et al. 2019; Pillepich et al. 2019). Each simulation has a companion dark matter-only (DMO) and an analogous full-physics (FP) run. The cosmological parameters used in each simulation are taken from Planck Collaboration et al. (2016), with matter density $\Omega_{M,0} = 0.3089$, baryon density $\Omega_{b,0} = 0.0486$, dark energy density $\Omega_{\Lambda,0} = 0.6911$, Hubble constant $H_0 = 67.74$ km s^{-1} Mpc^{-1}, power spectrum normalization factor $\sigma_8 = 0.8159$, and spectral index $n_s = 0.9667$.

TNG builds upon the original Illustris model (Vogelsberger et al. 2013; Torrey et al. 2014), which uses the AREPO code (Springel 2010) to solve coupled equations of self-gravity and magnetohydrodynamics (Pakmor et al. 2011; Pakmor & Springel 2013). To achieve improved consistency with observations, TNG refined the original Illustris models for active galactic nuclei (AGN) feedback, galactic winds, and magnetic fields (Weinberger et al. 2017; Pillepich et al. 2018a).

Several physical processes in TNG, such as star formation, stellar feedback, black hole seeding, black hole accretion, and AGN feedback, cannot be directly simulated due to resolution limitations and are thus implemented using 'sub-grid' recipes. The parameters for these sub-grid processes are calibrated to align with various observations, similar to the methodology used in SAMs. However, the specific observations and the precision of calibration differ. For TNG, calibration targets include the cosmic star formation rate density as a function of redshift, stellar mass functions, the relationship between black hole mass and stellar mass, the hot gas fraction in galaxy clusters, and the galaxy stellar mass versus radius relation (Pillepich et al. 2018a). Additionally, the distribution of galaxy optical colors in stellar mass bins was used to refine AGN feedback parameters, as detailed in Nelson et al. (2018). While these calibration choices overlap with those used for the SC SAM, described in the section below, there are differences in the specific observations and calibration techniques used.

Given that this paper focuses on low mass halos $M_{\rm halo} < 10^{12} M_\odot$, TNG's treatment of stellar feedback, particularly the treatment of supernova-driven galactic winds (Pillepich et al. 2018a), is most relevant for our study. Following the original Illustris simulation (Vogelsberger et al. 2013), in the TNG model, supernovae launch galactic winds from the dense ISM. The winds are modeled as collisionless particles ejected isotropically from star-forming gas cells. The rate of kinetic energy released from each cell is determined by a mass loading function, which depends on the gas phase metallicity and the dark matter velocity dispersion σ_{DM}. To measure σ_{DM}, a weighted kernel is used over the nearest 64 DM particles. The velocity imparted to the wind particles is also a function of σ_{DM} and redshift. These outflows are strong enough to remove mass from the ISM (Nelson et al. 2019), and, as we demonstrate in Section 3, push gas out of the halo.

In this paper, we use both the hydrodynamical (full-physics) and dark matter only (N-body) outputs of the intermediate-sized box ($L_{\rm box} = 75$ Mpc h^{-1}) at its highest resolution, TNG100-1.

2.2 The Santa Cruz semi-analytic model

The Santa Cruz SAM of galaxy formation, first introduced in Somerville & Primack (1999), and subsequently updated in Somerville et al. (2008a, 2012), Porter et al. (2014), Popping et al. (2014), and Somerville et al. (2015), traces the evolution of baryons within galaxies by partitioning them into four distinct reservoirs: the cold gas in the galaxy disk, the hot gas associated with the dark matter halo, the ejected gas reservoir, and the stellar component, the latter of which is further divided into disk and bulge populations. To model the mass and energy transfer between these reservoirs, the Santa Cruz SAM incorporates physically and observationally motivated prescriptions for a variety of baryonic processes. These include gas cooling, star formation, stellar feedback, gas recycling, chemical enrichment, and the growth of supermassive black holes and their associated feedback. In this work, we use the latest version of the Santa Cruz SAM published in Somerville et al. (2015) and referenced in Yung et al. (2023) and Gabrielpillai et al. (2022). Since we limit our focus to central galaxies with $M_{halo} < 10^{12}$, we turn AGN feedback "off" in the SAM. Below, we briefly summarize the key processes modeled in the SAM, and refer the reader to Somerville et al. (2008a) and Porter et al. (2014) for details.

2.2.1 *Gas Cooling and Accretion*

For any given halo, the SAM computes the dark matter accretion rate $\dot{m}_{\rm DM}$ by finite differencing the virial mass time series provided by the halo merger tree, discussed further in Section 2.3. Prior to reionization, the SAM assumes that gas accretion $\dot{m}_{\rm acc}$ closely follows the accretion of dark matter, scaled by the universal baryon fraction f_b as:

$$\dot{m}_{\rm acc} = f_{\rm b} \dot{m}_{\rm DM}. \tag{1}$$

where $f_{\rm b} = 0.1573$ (Planck Collaboration et al. 2016).

After reionization, the photoionizing background suppresses gas accretion. The fraction of baryons that can collapse into the halo is determined by $f_{\rm coll}$, which depends on halo mass and redshift (Okamoto et al. 2008). The SAM also incorporates the re-accretion of gas previously ejected from the halo due to stellar feedback, discussed further in Section 2.2.2, with the rate of re-accretion given by:

$$\dot{M}_{\rm CGM,in,recycled} = \chi_{\rm re-infall} \left(\frac{M_{\rm ejected}}{t_{\rm dyn}} \right), \tag{2}$$

where $M_{\rm ejected}$ is the total mass of the ejected gas reservoir and $\chi_{\rm re-infall}$ determines the fraction of ejected gas that can return to the hot halo at each time step. Typically, $\chi_{\rm re-infall} = 0.1$, resulting in the ejected gas returning over ~ 10 dynamical times, where the dynamical time is defined as $t_{\rm dyn} \equiv \frac{R_{\rm vir}}{V_{\rm vir}}$, and $V_{\rm vir}$ is the circular velocity of the halo at the virial radius. Additionally, when a halo becomes a subhalo, the SAM assumes that the subhalo's CGM is

	TNG100 Pillepich et al. (2018a); Springel & Hernquist (2003)	SC SAM Somerville et al. (2008a, 2015); Yung et al. (2019)	TNG SAM this paper
Box Size	$75\,h^{-1}$ Mpc	$75\,h^{-1}$ Mpc	$75\,h^{-1}$ Mpc
Particle Resolution	$m_{\rm DM} = 5.06 \times 10^6\ M_\odot/h$	$\mathrm{mass_{min}} = 8.85 \times 10^8\ M_\odot$	$\mathrm{mass_{min}} = 8.85 \times 10^8\ M_\odot$
Halo Gas Accretion	. . .	NFW	$f_{in}^{CGM} \propto f\,(M_{\rm halo}, z)$
Hot Halo Gas Re-incorporation	. . .	$\chi_{\rm re-infall} = 0.1$	bundled into f_{in}^{CGM}
Hot Halo Gas Cooling	. . .	$r_{\rm cool} < r_{\rm vir}$: cold mode accretion $r_{\rm cool} > r_{\rm vir}$: hot mode accretion	$t_{\rm cool} \propto f\,(M_{\rm halo}, z)$
Star Formation	Kennicutt-Schmidt; gas above density threshold forms stars; $\Sigma\mathrm{SFR} \propto \rho^{1.5}$; $\tau_{*,0} = 2.1$ Gyr; Chabrier IMF	multi-phase gas partitioning into neutral, ionized, and molecular components (Gnedin & Kravtsov 2011); H_2-based star formation recipe (Bigiel et al. 2008); $\tau_{*,0} = 1.0$ Gyr; Chabrier IMF	Kennicutt-Schmidt; gas above $\Sigma_{\rm crit} = 4.5\ M_\odot \mathrm{pc}^{-2}$ forms stars $\Sigma\mathrm{SFR} \propto \rho^{1.5}$; $\tau_{*,0} = 1.0$ Gyr; Chabrier IMF
Chemical Enrichment	delayed recycling; metals produced by AGB stars (1–8 $M_\odot$), SNII (8–100 $M_\odot$), and SNIa; yields for each source determined from rescaled yield tables; enrichment events discretized when mass fraction > 0.0001 or star age < 100 Myr	instantaneous recycling; fixed yield $y = 1.2$; $f_{\rm recycle} = 0.43$	instantaneous recycling; fixed yield $y = 2.0$; $f_{\rm recycle} = 0.43$
Stellar Feedback	originates from star-forming gas particles; Injection velocity $\propto$ [350 km s^{-1}, $f\,(\sigma_{DM}, H(z))$]; $\eta_{\rm ISM} \propto f\,(v_w, e_w)$	originates from scale of galaxy; SNe ejection efficiency $\epsilon_{\rm SN} = 1.7$, ejection scale $V_{\rm eject} = 110$ km/s; gas deposited in ejected reservoir	originates from scale of galaxy; $\eta_{\rm ISM} \propto f\,(v_w, e_w, M_{\rm halo}, z)$; gas deposited in hot halo; leftover SNe energy drives halo outflows (Henriques et al. 2015); $\eta_{\rm halo} \propto f\,(\eta_{\rm ISM}, M_{\rm halo}, z)$; gas deposited in ejected reservoir
Metal Circulation	metal loading of wind particles: $\gamma_w = 0.4$	metal flows carry the same metallicity as the source reservoir	metal flows carry metallicity $\propto f\,(M_{\rm halo}, z)$ of the source reservoir
Calibrations	metal loading of wind particles: $\gamma_w = 0.4$	metal flows carry the same metallicity as the source reservoir	metal flows carry metallicity $\propto f\,(M_{\rm halo}, z)$ of the source reservoir

Table 1. Overview of key parameters and analytic recipes in the TNG100 simulation, the Santa Cruz SAM and the newly developed TNG SAM. Key parameters highlighted include the simulation box size, resolution, black hole accretion and feedback, galactic wind models, star formation prescriptions, stellar evolution, chemical enrichment, and gas cooling and re-accretion processes.

instantly transferred to the host halo, contributing to the mass of the halo's hot gas reservoir.

Following the approach of White & Frenk (1991), the CGM is assumed to be uniformly at the virial temperature of the halo at each time step. The radiative cooling time, which represents the timescale for the gas to cool by radiating away its thermal energy, is computed using the cooling function $\Lambda(T_{\rm vir}, Z_{\rm h})$ (Sutherland & Dopita 1993), where $T_{\rm vir}$ is the virial temperature and $Z_{\rm h}$ is the metallicity of the hot halo gas. The gas density profile is assumed to follow a singular isothermal sphere. Integrating the cooled mass within the radius $r_{\rm cool}$, which is the radius within which all of the gas can radiatively cool within the cooling time $t_{\rm cool}$, yields the ISM mass accretion rate.

When $r_{\rm cool}$ is smaller than the virial radius $r_{\rm vir}$, the SAM applies a standard cooling flow model. The cooling time $t_{\rm cool}$ is calculated using the formulation in Somerville et al. (2008a), assuming an isothermal and isobaric gas density profile. If $r_{\rm cool}$ exceeds $r_{\rm vir}$, the cooling rate is equivalent to the gas accretion rate into the halo. Notably, instances where $r_{\rm cool}$ exceeds $r_{\rm vir}$ represent the "cold/fast/filamentary" mode accretion. The SAM ignores the radiative cooling prediction during these time steps, setting the ISM accretion rate equal to the halo gas accretion rate. Various modifications within this cooling model, such as alternative definitions of the cooling time or changes to the gas density profile, can introduce variations in the ISM accretion rate by a factor of approximately 2-3 (Somerville et al. 2008b).

2.2.2 Star Formation and Stellar Feedback

All star formation recipes available for use in the SAM generally follow the form given by:

$$m_* = \frac{m_{\rm cold}}{\tau_*}, \tag{3}$$

where τ_* is an adjustable efficiency parameter, typically a constant. In the most recently used Santa Cruz SAM, gas accreted into the ISM is partitioned into H I, H_2, H II, and metals, with their respective mass surface densities tracked in radial disk annuli (Popping et al. 2014; Somerville & Davé 2015). The default prescription for the star formation rate (SFR) surface density is based on the molecular hydrogen gas phase alone, accounting for a higher conversion efficiency above a critical H_2 surface density (Bigiel et al. 2008; Narayanan et al. 2012):

$$\dot{\Sigma}_{\rm SFR} = A_{\rm SF}\left(\frac{\Sigma_{H_2}}{10M_\odot{\rm pc}^{-2}}\right)\left(1+\frac{\Sigma_{H_2}}{\Sigma_{\rm H_2,crit}}\right)^{N}_{\rm SF}, \tag{4}$$

where A_{SF}, N_{SF} and $\Sigma_{\rm H_2,crit}$ are free parameters. We set A_{SF} = $5.98\times10^{-3}M_\odot{\rm yr}^{-1}{\rm kpc}^{-2}$, N_{SF} = 1.0 and $\Sigma_{\rm H_2,crit} = 70M_\odot{\rm pc}^{-2}$, following Popping et al. (2014, 2019). In the SAM, the default setting for estimating the molecular hydrogen gas density Σ_{H_2} uses the metallicity-dependent partitioning approach of (Gnedin & Kravtsov 2011).

In the SAM, stellar feedback ejects cold gas from the ISM, with the ejection rate modeled as a power law:

$$\dot{m}_{\rm eject} = \epsilon_{\rm SN}\left(\frac{200{\rm km/s}}{V_{\rm disk}}\right)^{\alpha_{\rm rh}}\dot{m}_*, \tag{5}$$

where the free parameters $\epsilon_{\rm SN}$ and $\alpha_{\rm rh}$ modulate the efficiency and dependence on the disk's circular velocity $V_{\rm disk}$, and $\dot{m}_*$ is the star formation rate. $V_{\rm disk}$ is approximated as the circular velocity of the uncontracted halo at twice the Navarro-Frenk-White (NFW) scale radius r_s (Navarro et al. 1996). All ejected gas is expelled from the halo entirely and deposited in the "ejected" reservoir. A fraction of this gas is allowed to return to the hot halo on dynamical timescales, as described in Section 2.2.1.

2.2.3 *Metal Production*

The Santa Cruz SAM employs the instantaneous recycling model for metal production, a common method in SAMs. When a mass of stars, dm$_*$, forms, it produces a corresponding mass of metals, dM$_{\rm Z}$ = y · dm$_*$, which are immediately mixed with the cold gas in the disk. The yield, y, is typically tuned to match observational data, such as the normalization of the stellar metallicity versus mass relation from Gallazzi et al. 2005, as in Somerville et al. 2015. While most other SAMs derive the yield from stellar evolution models, which are also based on observational constraints, the Santa Cruz SAM's approach offers a simpler alternative for calibration, particularly given the crude nature of the instantaneous recycling approximation. The cold gas metallicity, $Z_{\rm cold}$, is tracked over time, with new stars inheriting this metallicity. Supernova feedback ejects both metals and gas from the disk, mixing them into the hot halo or expelling them into an external reservoir at rates proportional to the outflowing gas mass. These ejected metals can later be re-accreted into the halo, contributing to further chemical enrichment.

2.2.4 *Observational Calibration*

The SC SAM is calibrated by adjusting free parameters to match key observations at $z\sim0$, such as the stellar-to-halo mass relation, stellar mass function, stellar mass-metallicity relation, cold gas fraction versus stellar mass for disk-dominated galaxies, and the black hole mass vs. bulge mass relation. Observational constraints for these calibrations are sourced from Rodríguez-Puebla et al. (2017), Bernardi et al. (2013), Gallazzi et al. (2005), Peeples et al. (2014), Calette et al. (2018), and McConnell & Ma (2013). Additional cross-checks involve the cold gas phase mass-metallicity relation and the H_2 mass function, using constraints from Obreschkow et al. (2009), Keres et al. (2003), Anderson et al. (2014), Zahid et al. (2013), and Boselli et al. (2014). The calibration considers the sensitivity of gas fraction, stellar metallicity, and star formation efficiency, fine-tuning the parameters to balance these observational constraints while adjusting for the effects of AGN and SNe feedback to match both high-mass and low-mass galaxy populations. For a more detailed description of the observations used for calibration, refer to Appendix B in Yung et al. (2023).

2.2.5 *New Modifications made to the Santa Cruz SAM*

The version of the Santa Cruz SAM presented in this work revises how the SAM computes the rate of gas condensation from the CGM into the ISM. When $r_{\rm cool} > r_{\rm vir}$, the original Santa Cruz SAM disregards the radiative cooling prediction and equates the ISM accretion rate to the halo gas accretion rate. This approach, however, leads to unrealistically low hot halo gas masses in dwarf galaxies (Pandya et al. 2020). To rectify this issue, we follow Pandya (2021) and adopt a modified approach inspired by Guo et al. (2011): when $r_{\rm cool} > r_{\rm vir}$, the rate of cooling is limited solely by the freefall time of the hot halo gas, such that:

$$\dot{M}^{\rm in}_{\rm ISM} = \begin{cases} \frac{M_{\rm CGM}}{t_{\rm dyn}}\frac{r_{\rm cool}}{r_{\rm vir}} & \text{when } r_{\rm cool} < r_{\rm vir} \\ \frac{M_{\rm CGM}}{t_{\rm dyn}} & \text{when } r_{\rm cool} \geq r_{\rm vir}. \end{cases} \tag{6}$$

While this modification no longer predicts extremely low CGM masses in dwarf galaxies (see Appendix B), it has its own limitations. The new scenario when $r_{\rm cool} > r_{\rm vir}$ suggests that additional gas external to the halo, possibly in the form of cold IGM filaments, is contributing to the accretion process. Thus, the freefall-limited accretion rate might represent a lower bound, and a more complete model should incorporate contributions from both cold and hot accretion modes.

2.3 Matching Galaxies Between TNG FP and SC SAM Run on TNG-DMO

The precise identification of halos and construction of merger trees forms the backbone of all SAMs. Thus, to facilitate a direct comparison between the Santa Cruz SAM and TNG, we must use reasonably similar merger trees. The SC SAM employs the ROCKSTAR halo finder and CONSISTENT TREES, a gravitationally consistent merger tree algorithm developed by Behroozi et al. (2012), to extract merger trees from the Bolshoi cosmological N-body simulation (Klypin et al. 2011). TNG, however, utilizes a different halo finder based on the friends-of-friends (FoF) algorithm (Davis et al. 1985) to identify "groups," and the SUBFIND algorithm (Springel et al. 2001) to identify substructure.

To create bijective matches between the two sets of halo catalogs, Gabrielpillai et al. (2022) ran the ROCKSTAR halo finder and CONSISTENT TREES on TNG100-1-DM. They then matched halos identified by ROCKSTAR and SUBFIND catalogs with SubLink, a software tool developed by Rodriguez-Gomez et al. (2015) that uses a merit function for matching subhalos. This produced successful

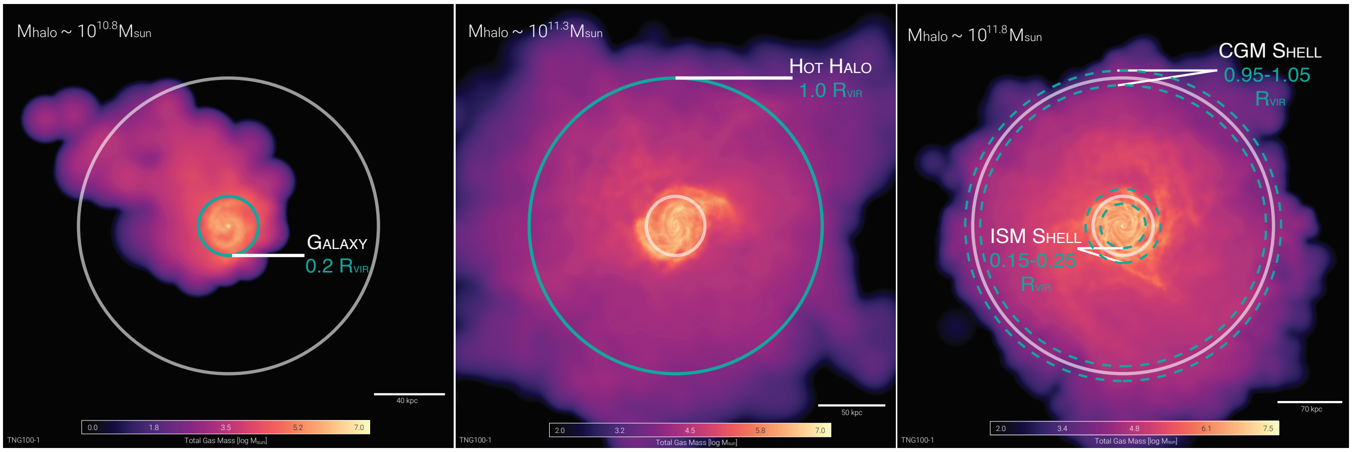

Figure 1. Three halos from TNG100, spanning the $10^{10.5} - 10^{12} M_{\odot}$ mass range analyzed in this work, are shown to demonstrate how TNG's outputs are compared to the SAM. The maps are color-coded by total gas mass, with brighter regions indicating higher mass concentrations. The "galaxy" is defined as all material within 0.1 $r_{\rm vir}$(left panel, green circle), and the "halo" as all material within $r_{\rm vir}$(center panel, green circle). To analyze the flow of baryons at the galactic and halo scales, we examine inflow and outflow rates within the boundaries highlighted by dashed green circles in the right panel: 0.05-0.15 $r_{\rm vir}$for the galaxy and 0.95-1.05 $r_{\rm vir}$for the halo. updating figure

bijective matches between the ROCKSTAR and FoF/SUBFIND halos for central galaxies, achieving a 99% match rate. The fraction of bijective matches for non-central subhalos, however, is often substantially lower, with a match rate from 50–70%. As a result, we limit our analysis to central galaxies only.

Although > 99% of central galaxies have bijective matches, a direct comparison between the halo mass of the central galaxies between the two catalogs, however, reveals slight offsets up to 20% for low mass halos (see Figure 2 in Gabrielpillai et al. (2022)). These discrepancies are likely primarily influenced by baryonic physics rather than differences in halo-finding algorithms. For a more detailed description of the halo finder, merger tree algorithms, and method used to create these bijective matches, we refer the reader to Section 3 of Gabrielpillai et al. (2022).

2.4 Selecting Comparable Galaxy and Halo Properties

To make reliable comparisons between the output from TNG and the SAM, we identify comparable quantities at the scale of the galaxy and the scale of the halo. As illustrated in the left and middle panels of Figure 1, we define the galaxy as all material within 0.2 $r_{\rm vir}$and the halo as all material within $r_{\rm vir}$. Properties at the "halo scale" include the virial mass ($M_{\rm halo}$), the mass of the hot halo ($M_{\rm hot}$), the metallicity of the gas in the hot halo ($Z_{\rm hot}$), and the overall baryon fraction ($f_{\rm baryon}$). Properties at the "galaxy scale" describe the stellar mass ($M_{\rm star}$), cold gas mass ($M_{\rm cold}$), their respective metallicities ($Z_{\rm star}$ and $Z_{\rm cold}$), and the star formation rate of the central galaxy within the halo. We define the baryon fraction as the sum of $M_{\rm cold}$, $M_{\rm star}$, and $M_{\rm hot}$ divided by the total halo mass. Although the SC SAM stores mass in an ejected reservoir as well, we do not count this mass towards the overall baryon fraction.

In TNG, we define the CGM as all gas within the FoF halo, excluding the gas contribution from each galaxy within the same halo. The galaxy is defined as all matter within twice the stellar half-mass radius (SHMR). In the SAM, the CGM consists of gas accreted into the halo and ejected from galaxies, making it directly comparable to TNG's definition. However, the definition of the galaxy, particularly its cold gas component ($M_{\rm cold}$), is less straightforward. In the SAM, cold gas is explicitly tracked via gas partitioning, whereas in TNG, this mass is not directly provided within twice the SHMR. For consistency, we define $M_{\rm cold}$in both TNG and the SAM as the total gas mass of the galaxy.

To compare these properties effectively, we require that all TNG halos be adequately resolved, given the finite mass resolution of the simulation. The mass resolution in the SAM is determined by the resolution of the N-body simulation used to extract the merger trees. Gabrielpillai et al. 2022 adopt the general guideline that a halo should contain at least 100 particles to be well resolved, and that the root halo should be at least 100 times the mass of the smallest progenitor that can be resolved in order to accurately resolve the halo's merger history. For TNG100-1-Dark, the mass resolution is $8.9 \times 10^6\ M_{\odot}$, leading Gabrielpillai et al. 2022 to adopt a conservative minimum root halo mass of approximately $8.9 \times 10^8\ M_{\odot}$. We adopt the same framework in this paper.

For the hydrodynamical TNG100-1, the target baryon mass is $1.4 \times 10^6\ M_{\odot}$, meaning that the mass of gas in each cell is maintained within a factor of two of this value, as is the mass of star particles at birth (Pillepich et al. 2018b). We restrict our analysis to TNG galaxies that have a minimum of approximately 100 stellar particles $M_{\rm star} \geq 1.4 \times 10^8\ M_{\odot}$, and 100 gas particles $M_{\rm gas} \geq 1.4 \times 10^8\ M_{\odot}$. Our minimum requirement for the gas particles naturally sets a lower limit on the SFR. Based on the analysis by Donnari et al. (2019), we adopt a minimum SFR of $1.0 \times 10^{-3}\ M_{\odot}\ {\rm yr}^{-1}$. Applying this filter allows us to resolve 19,650 galaxies with halo masses ranging from $\sim 4 \times 10^{10} - 10^{12} M_{\odot}$ at $z = 0$.

2.4.1 Flow Cycle Measurements in TNG

To establish a common language for describing the baryon cycle between TNG and the SC SAM, one must carefully analyze the gas flows in TNG. TNG, however, does not directly provide measurements of the rates of gas inflow and outflow within and around the galaxy. To address this, Cohen et al., in preparation (hereafter CIP), have extracted these measurements for a subset of ~ 1000 central galaxies in TNG100-1.

Using an Eulerian approach, CIP calculated instantaneous gas flows by defining volumetric shells of thickness $\Delta r \sim 0.05\ r_{\rm vir}$ and tracking the mass and velocity of gas crossing these boundaries between consecutive simulation outputs. The measurements were tracked coarsely in redshift-space at $z = \{0, 0.1, 0.2, 0.3, 0.5, 0.7, 1.0, 2.01, 3.01, 4.01, 5.01, 6.01\}$. For fur-

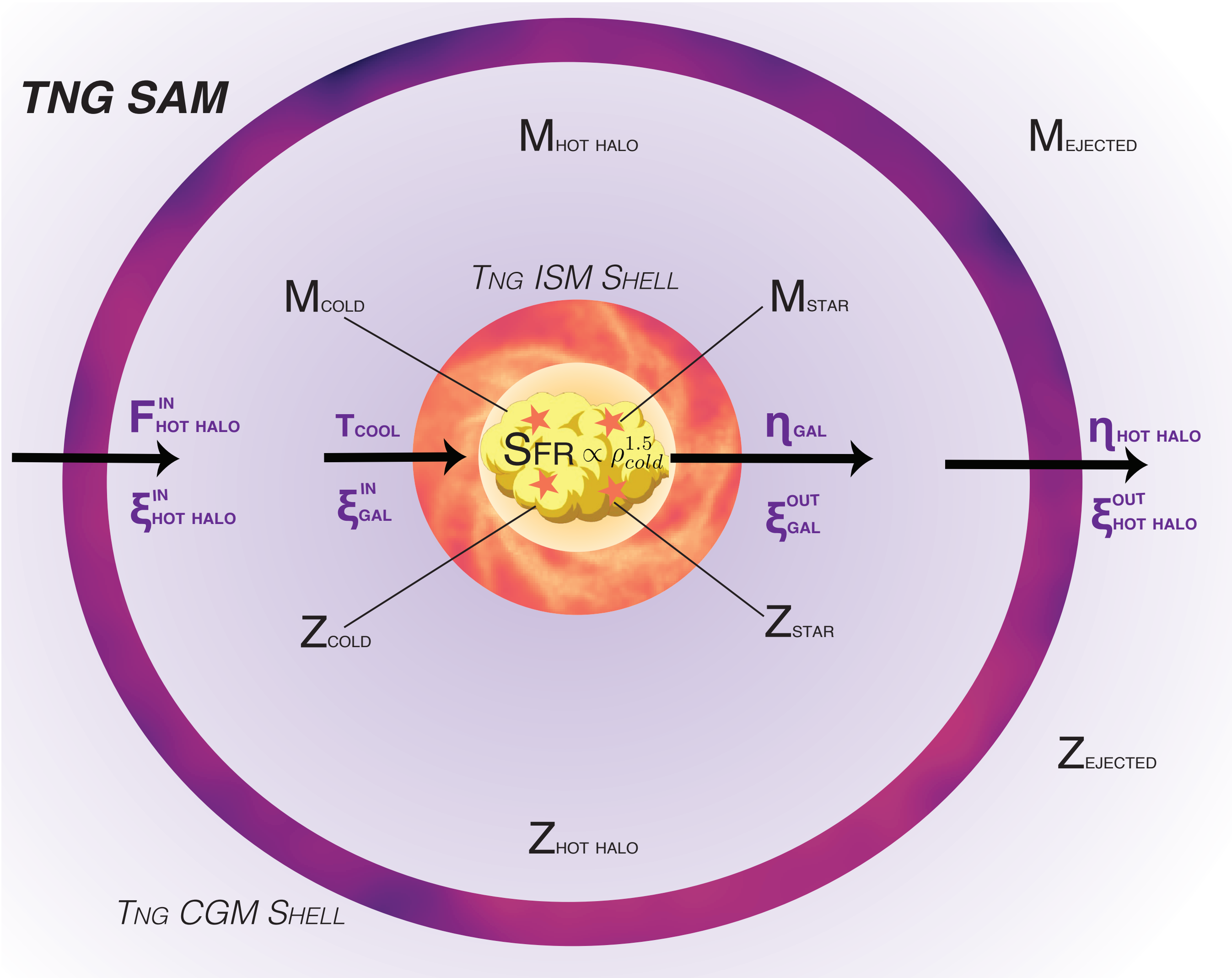

Figure 2. Illustration of the newly developed TNG SAM, calibrated to reproduce the baryon cycle of a sample of ~ 400 central galaxies in the TNG100 simulation. The diagram shows the main baryonic reservoirs—cold star-forming gas ($M_{\rm cold}$), stars ($M_{\rm star}$), hot halo gas ($M_{\rm hot\ halo}$), and ejected gas ($M_{\rm ejected}$)—and the physical processes governing the flows of gas and metals between them. Arrows represent the direction of baryon flow, either into or out of a given reservoir, with the parameter governing the direction of gas/metal flow labeled in purple above/below each arrow. For example, cooling from the hot halo into the ISM is governed by the cooling time ($t_{\rm cool}$), while $\eta_{\rm ISM}$ and $\eta_{\rm halo}$ modulate how efficiently stellar feedback drives gas outflows from the ISM and halo into the ejected reservoir. Metallicity enrichment is tracked for each reservoir, represented as $Z_{\rm cold}$, $Z_{\rm star}$, $Z_{\rm hot\ halo}$, and $Z_{\rm ejected}$. Each governing parameter was calibrated using the gas and metal inflow and outflow rates measured at the boundaries shown in the right panel of Figure 1. By incorporating these hydrodynamical insights, the TNG SAM aims to not only accurately reproduce the global galaxy and halo-scale properties modeled in TNG but also capture the underlying baryon cycle within a simplified semi-analytic framework.

ther details on the methodology and the specific tools and algorithms used to achieve these measurements, we refer the reader to Cohen et al., in preparation.

We further divide the CIP “flow" sample into “resolved" vs. “unresolved" categories. The resolved subsample comprises ~ 400 galaxies at each redshift, after applying the resolution criteria described in Section 2.4, at each redshift. We describe the remaining galaxies as the unresolved subsample. For the galaxies in each sample, we define the halo boundary as the region between $0.95 - 1.05\ r_{\rm vir}$, and the galaxy boundary from $0.1 - 0.2\ r_{\rm vir}$. Both boundaries are illustrated as dashed circles in the right panel of Figure 1. We volumetrically sum the inflow and outflow rates within each boundary, providing a basis for comparing gas flows in TNG to those in the SAM.

3 TRANSLATING TNG’S DETAILED PHYSICS INTO THE SC SAM’S GALAXY FORMATION MODEL

To translate the complex physics of a hydrodynamical simulation like TNG into the SC SAM’s simplified framework, we focus on modeling how the baryon cycle—how gas and metals move between the galaxy and its surrounding environment (halo)—evolves over time. We first take the inflow and outflow rates of gas and metals from the sample of TNG galaxies described in Section 2.4.1. Treating this sample as representative of the entire TNG central galaxy population, we derived physical parameters that govern the evolution of these flows, namely halo (re)-accretion efficiency, cooling time, and mass and metal loadings. For galaxy sizes, we use the full TNG100 dataset. These measurements, each shown in Figure 3 as they evolve with halo mass and redshift, form the basis for calibrating the SC SAM to reflect the baryonic processes observed in TNG.

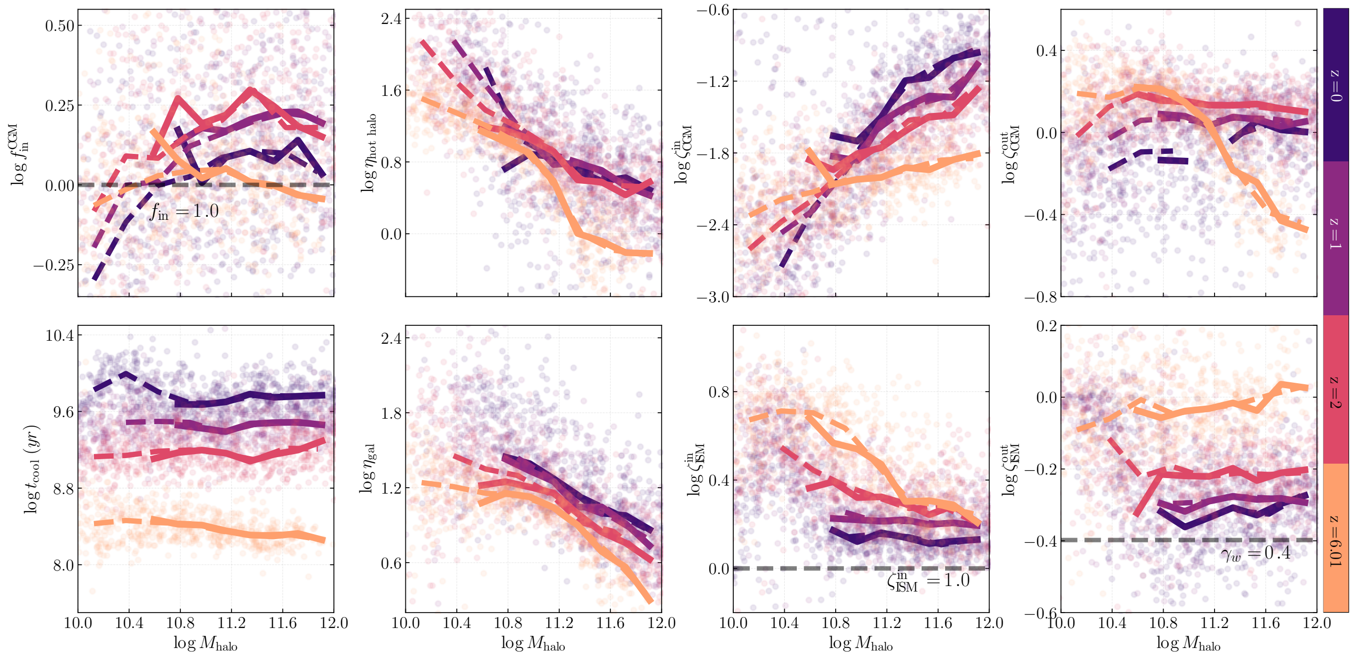

Figure 3. 3 by 3. missing kennicutt schmidt Overview of the physical parameters measured from the full TNG100 sample (solid lines) and the subset of TNG100 galaxies described in Section 2.4.1 (dashed lines), each directly input into the TNG SAM. Each panel plots the median (50th percentile) values for these parameters as a function of halo mass at select redshifts ($z = 0, 2, 6$), with each redshift represented by a different shade of blue. Analytic functions for each parameter, accurate to within $\sim 30\%$, are provided in the Appendix A.

needs to be cleaerTo implement these scaling relations in the SAM, we adopt a two-pronged approach leveraging the "resolved" and "unresolved" samples of TNG galaxies. For halos within the well-resolved mass range of $10.5 < \log M_{\rm halo} < 12$, we directly apply the derived scaling relations shown as solid lines in Figure 3. However, as we move backward in time, the majority of these galaxies' halo masses fall below our well-resolved limit. Instead of modeling these low-mass galaxies using only the resolved sample, we extrapolated scaling relations from the entire TNG and CIP samples (without mass resolution cuts), down to the SAM's minimum mass resolution. In the case of the CIP sample, the lowest halo mass probed is $\log M_{\rm halo} = 10$. Here, we extrapolate down to low halo masses based on the behavior of the galaxies from $10 < \log M_{\rm halo} < 10.5$, shown as dashed lines in Figure 3. This extrapolation allows us to infer the behavior of lower-mass galaxies, even though they are not directly resolved by the flow measurements.

In the newly calibrated SAM, we apply these scaling relations across halo mass and time, performing linear interpolation to determine the relations at intermediary halo masses and redshifts. While the physical processes governing gas flows are not expected to fundamentally change with redshift, TNG reveals an evolving behavior over time, likely driven by underlying physical mechanisms that remain poorly understood. We bundle this ignorance into our interpolation approach, providing a pragmatic approximation of TNG's redshift-dependent behavior. We also provide analytic functions of halo mass and redshift that capture each relation within 20% accuracy in Appendix B. This approach, as opposed to directly inserting flow rates extracted from TNG, allows the SAM to calculate the flow rates self-consistently based on the given physical parameters, ensuring a more physically motivated and flexible SAM. We refer to this newly calibrated model, illustrated in Figure 2, as the 'TNG SAM.'

3.1 Halo Accretion and Cooling

3.1.1 IGM - CGM Accretion and Recycling

In the traditional SAM framework, the rate at which gas accretes onto the CGM is tightly coupled to the dark matter accretion rate, as detailed in Section 2.2.1. In the new TNG SAM, we introduce the parameter $f_{\rm in,CGM}$ to regulate the total gas inflow into the CGM:

$$f_{\rm in,CGM} \equiv \dot{M}_{\rm in,CGM} / (f_b \, \dot{M}_{\rm halo}), \tag{7}$$

Here, $f_{\rm in,CGM}$ measures the efficiency of gas accretion compared to the expected baryonic inflow, where we do not distinguish between pristine and recycled gas. $\dot{M}_{\rm in,CGM}$ is the gas mass inflow rate into the CGM, f_b is the cosmic baryon fraction, and $\dot{M}_{\rm halo}$ is the to the *net* mass accretion rate of the halo in TNG. elaborate on the net

When $f_{\rm in,CGM} = 1$, the inflow rate matches the expected baryon-to-dark matter ratio. Values below 1 indicate reduced inflow, while values above 1 suggest enhanced inflow efficiency. The top left panel of Figure 3 shows that in TNG, $f_{\rm in,CGM}$ fluctuates at or above unity across halo mass and redshift, indicating that the gas inflow generally meets or exceeds the expected baryonic fraction. We further explore the implications of this behavior in Section 5.1.1.

3.1.2 CGM-ISM Cooling

At the scale of the galaxy, the SC SAM, like most conventional SAMs, relies on the cooling radius $r_{\rm cool}$ to determine the rate at which gas cools into the ISM, as described in Section 2.2.1. In the traditional model, the "cooling time" $t_{\rm cool}$, i.e. the time needed for the gas to cool, is calculated assuming an isothermal, isobaric gas density profile. In "cold" mode accretion ($r_{\rm cool} > r_{\rm vir}$), gas cools rapidly and falls directly into the galaxy, so the cooling time scales with the dynamical time. Conversely, in "hot" mode accretion ($r_{\rm cool} < r_{\rm vir}$), the hot halo gas is shock-heated and the cooling time is significantly longer.

In TNG, we define the cooling time as

$$t_{\rm cool} \equiv M_{\rm hot}/\dot{M}_{\rm cool,CGM-ISM}, \tag{8}$$

where $\dot{M}_{\rm cool,CGM-ISM}$ describes the rate that gas cools from the hot halo into the ISM. The left middle panel of Figure 3 shows the resulting cooling times as a function of halo mass and redshift. We find that the cooling times consistently exceed the dynamical time across all halo masses explored, implying that the "cold" vs. "hot" mode dichotomy does not adequately describe the rate of cooling in TNG, discussed further in 5.1.2. In the new TNG SAM, we use the cooling times observed in TNG to determine the rate at which gas accretes onto the galaxy by rearranging Equation 8.

3.2 Star Formation

In TNG, star formation occurs below the mass resolution and is thus treated using a subgrid model. Specifically, the TNG model adopts the two-phase ISM model of Springel & Hernquist (2003), where gas cells above the density threshold $\Sigma_{\rm gas}$ are split into cold star-forming clouds and hot ionized gas. Star formation is then computed in equilibrium, with the SFR proportional to the cold gas density and scaled by an adjustable free-fall time $t_{*,0}$, which is tuned to reproduce global observed Kennicutt-Schmidt relation, given by Kennicutt (1998) as:

$$\Sigma_{\rm SFR} = (2.5{\pm}0.7){\times}10^{-4}\left(\frac{\Sigma_{\rm gas}}{M_\odot,{\rm pc}^{-2}}\right)^{1.4\pm0.15} M_\odot,{\rm yr}^{-1},{\rm kpc}^{-2}. \tag{9}$$

Instead of the power law index $n = 1.4$, the TNG model applies a scaling of SFR $\propto \rho^{n=1.5}$ such that the hydrodynamics roughly reproduce the observed KS relation across the global scale of individual galaxies.

In the new TNG SAM, we also implement the KS relation, but at the scale of the entire galaxy, and with the goal of reproducing the aggregate Kennicutt Schmidt relation of TNG galaxies. Consistent with the recipe used in previous versions of the Santa Cruz SAM (Somerville et al. 2008a, 2012, 2015), the KS relation is applied to the total surface density of the cold neutral gas, which includes both atomic and molecular components. Star formation only occurs when the gas surface density exceeds a critical threshold, after which the star formation rate density is computed using the KS relation given in Equation 9, but with the slope set to 1.5 as done in TNG, and with a normalization free parameter $A_{\rm SF}$.

The KS relation's dependence on gas surface density necessitates consistent definitions of disk sizes in the SAM and TNG. As outlined in Section 2.4, we adopt a uniform definition for the galaxy radius, setting it to 0.1 $r_{\rm vir}$in both models. With disk sizes aligned, we find that we reproduce the median global KS relation in TNG within 10% after setting $A_{\rm SF} = 1.66667 \times 10^{-4}$ and $\Sigma_0 = 4.5$, as illustrated in Figure 3

3.3 Stellar Feedback

3.3.1 Galactic Winds and Galaxy-scale Outflows

To emulate TNG's treatment of stellar feedback, the TNG SAM incorporates the galactic wind model from (Pillepich et al. 2018b). Inspired by the results of semi-analytic models, the TNG model launches wind particles with an initial speed that scales with the local dark matter velocity dispersion $\sigma_{\rm DM}$. It also includes a redshift-dependent factor and a minimum wind velocity, such that the wind velocity v_w scales as:

$$v_w = \max\left[\kappa_w \sigma_{\rm DM}\left(\frac{H_0}{H(z)}\right)^{1/3}, v_{w,\rm min}\right] \tag{10}$$

where $\kappa_w = 7.4$ and $v_{w,\rm min} = 350$ km s^{-1}in the fiducial TNG model. This form ensures a physically plausible scaling of wind velocities with redshift and halo mass, while preventing unphysically large mass loading factors in low-mass halos.

The TNG model further refines wind generation by linking the wind mass loading factor η_w to the specific energy available for wind generation e_w. This energy is primarily determined by the energy released from Type II supernovae, with a fraction (τ_w) being thermal. The wind energy itself is a function of the metallicity of the star-forming gas, leading to a metallicity-dependent galactic wind model.

The wind mass loading factor, defined as the ratio of the mass outflow rate $\dot{m}_{\rm ISM,out}$ to the star formation rate $\dot{m}_*$, quantifies the efficiency of these winds in removing gas from the ISM. η_w is related to $v_{\rm W}$ and the wind energy, e_w, as:

$$\eta_w = \frac{2}{{v_w}^2}\, e_w(1-\tau_w) \tag{11}$$

where e_w is given by:

$$e_w = \bar{e}_w\left[f_{w,Z} + \frac{1-f_{w,Z}}{1+(Z/Z_{\rm w,ref})^{\gamma_{w,Z}}}\right] \times N_{\rm SNII} E_{\rm SNII,51}\, 10^{51} {\rm erg\, M_\odot^{-1}} \tag{12}$$

Here, $\bar{e}w$ is the average energy per unit stellar mass formed, fw, Z modulates the metallicity dependence, Z represents the gas metallicity, $Z_{\rm w,ref}$ is a reference metallicity, $\gamma_{w,Z}$ controls the strength of the metallicity dependence, $N_{\rm SNII}$ denotes the number of Type II supernovae, and $E_{\rm SNII,51}$ is the energy released per supernova in units of 10^{51} erg.

In the TNG model, η_w is implemented at the scale of the launched wind particle. To implement this model within the TNG SAM, we instead apply η_w at $R_{\rm disk}$. However, the left panel of Figure 4 shows that the value of η at the scale of the galaxy (solid lines) almost consistently the value at launch (dashed lines), indicating that the winds entrain additional material as they propagate outwards. To account for this in the SAM, we model the ratio of η_w at the site of the launched wind particle to η_w at the scale of the galaxy in TNG, shown in the middle panel of Figure 3. Since the TNG SAM applies η_w at the scale of the disk, the material ejected from the ISM is always deposited in the CGM.

3.3.2 Halo-scale Outflows

In TNG, galactic winds not only expel gas from the galaxy but also entrain additional material from the CGM, ejecting it into the IGM. In the SC SAM, however, stellar feedback drives gas directly from the ISM into an ejected reservoir, bypassing the CGM. The ejected gas only reconnects with the CGM indirectly, when a portion of it is re-accreted into the hot halo at later times. In the new TNG SAM, we explicitly account for the CGM-IGM outflow channel with the parameter $\eta_{\rm halo}$, defined as the ratio of the mass outflow rate $\dot{m}_{\rm CGM,out}$to the star formation rate $\dot{m}*$. Complementing the existing η_w, $\eta_{\rm halo}$ quantifies the efficiency with which stellar feedback ejects gas from the halo.

The model for $\eta_{\rm halo}$in the TNG SAM is inspired by the halo-scale outflow model used in the L-galaxies galaxy formation model for the

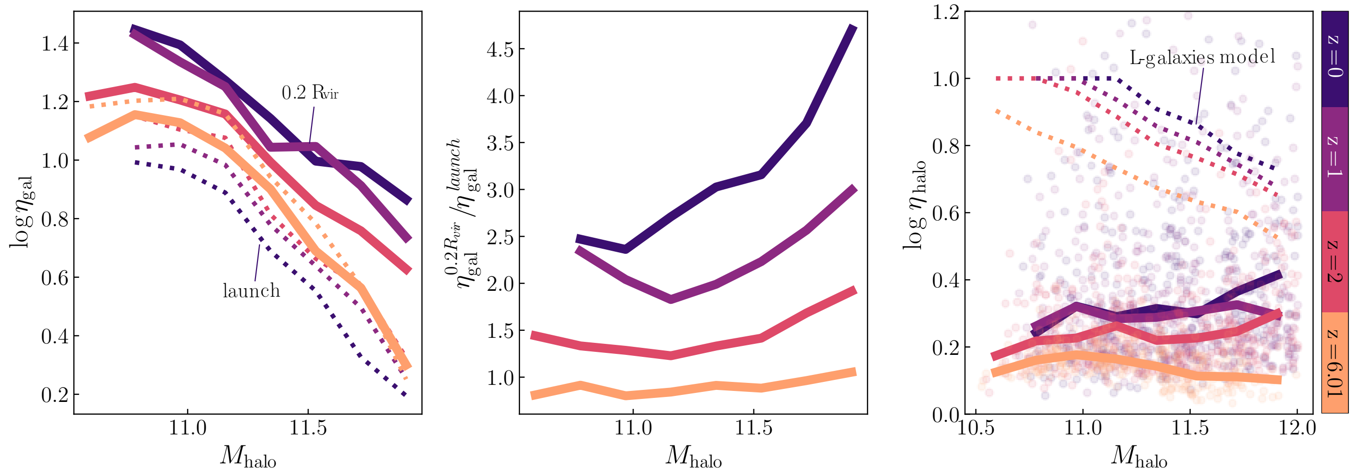

Figure 4. How the TNG SAM models the strength of stellar feedback-driven outflows at the scale of the galaxy (left panels) and the scale of the halo (right panel). The left panel shows that at the scale of the galaxy, $\eta_{\rm ISM}$(solid lines) typically exceeds the value launched from the star-forming gas cell in TNG (dashed lines), suggesting additional entrainment by he time the winds reach the galaxy's radius. To account for this, the TNG SAM scales the launch value by the ratio of the value at the scale of the galaxy to to at launch, as shown in the middle panel. At the scale of the halo, we model the efficiency of $\eta_{\rm halo}$using the dimensionless parameter $\epsilon_{\rm halo}$, introduced in the L-galaxies semi-analytic model. The best-fit values derived from the L-galaxies SAM (dashed lines), however, do not align with the behavior observed in TNG. We therefore calculate the strength of $\epsilon_{\rm halo}$ directly in TNG instead (solid lines) using $\eta_{\rm halo}$and $\eta_{\rm ISM}$.

Millenium simulations (Henriques et al. (2015); H15 hereafter). In the H15 model, surplus energy from supernovae, after reheating gas within the ISM and driving it into the CGM, can further expel the hot halo gas into the IGM as:

$$\frac{1}{2}\Delta m_{\rm eject}V_{\rm vir}^2 = \Delta E_{\rm SN} - \Delta E_{\rm reheat}, \tag{13}$$

where $\Delta E_{\rm reheat} = \frac{1}{2}\Delta m_{\rm reheat}V_{\rm vir}^2$.

By assuming the quantity $\Delta m_{\rm eject}/\Delta m_*$ is equivalent to our $\eta_{\rm halo} \equiv \dot{m}_{\rm CGM-IGM}/\dot{m}_*$, we derive the expression for $\eta_{\rm halo}$ as:

$$\eta_{\rm halo} = \frac{2\epsilon_{\rm halo}V_{\rm SN}^2}{V_{\rm vir}^2} - \eta_{\rm ISM} \tag{14}$$

where $V_{\rm SN} = 630$ km/s is a constant and $\epsilon_{\rm halo}$ is a dimensionless efficiency parameter capped at unity and is given by:

$$\epsilon_{\rm halo} = \epsilon_{\rm halo,0}\left[0.5 + \left(\frac{V_{\rm max}}{V_{\rm eject}}\right)^{-\beta_2}\right]. \tag{15}$$

In H15, the best fit values for $\epsilon_{\rm halo}$ are $\epsilon_{\rm halo,0} = 0.62$, $\beta_2 = 0.80$, and $V_{\rm eject} = 100$km/s. The right panel of Figure **??**, however, shows that applying these values in TNG (dashed lines) leads to significantly stronger $\epsilon_{\rm halo}$ values than actually observed (solid lines), overestimating the efficiency by up to a factor of 10. In the TNG SAM, we parameterize $\epsilon_{\rm halo}$ using the values observed in TNG across halo mass and redshift.

All gas ejected from the halo enters the ejected reservoir and is not allowed to re-accrete. However, in the TNG SAM implementation, the $f_{\rm in,CGM}$ parameter accounts for some of this gas being re-accreted, though the reaccretion process itself is not modeled explicitly due to our inability to distinguish between pristine and recycled gas.

3.4 Metal Enrichment and Circulation

In TNG, metals not only trace star formation and chemical enrichment, but also crucially modulate the strength of galactic winds and cooling rates. The TNG model tracks the return of metals over time from asymptotic giant branch (AGB) stars, core-collapse supernovae (SNII), and Type Ia supernovae (SNIa), allowing it to follow how metals are gradually released and redistributed within the ISM and CGM. In contrast, the SC SAM adopts a simplified, instantaneous model for metal production and circulation, detailed in Section 2.2.3.

To account for the detailed metal circulation observed in TNG, we introduce metallicity-weighted mass-loading factors (or "metal-loadings") into the TNG SAM. These factors quantify the fraction of metals transported by gas flows relative to the total gas flow. Following Peeples & Shankar (2011), we compute the metal loadings to quantify the fraction of metals transported out of the ISM/CGM as follows:

$$\zeta_{\rm out} = \frac{\dot{M}_{\rm Z,out}}{\dot{M}_{\rm out}\cdot Z_{\rm gas}}, \tag{16}$$

where $\dot{M}_{\rm Z,out}$ is the rate at which metals are outflowing from the ISM or CGM, $\dot{M}_{\rm outISM/CGM}$ is the rate at which all gas is outflowing from the ISM/CGM, and $Z_{\rm gas}$ describes the metallicity of the gas reservoir from which the outflows stem.

Traditionally, the SC SAM assumed a $\zeta_{\rm out,ISM/CGM}$ value of unity, meaning that the metal component of the outflowing gas was directly proportional to the metallicity of the ISM/CGM. However, the two lower right panels in Figure 3 show that this assumption is not valid in TNG. At the CGM scale, $\zeta_{\rm out,CGM}$ often deviates from unity, decreasing significantly at higher redshifts. At the ISM scale, $\zeta_{\rm out,ISM}$ consistently falls below unity, indicating that the winds eject fewer metals relative to the average metallicity of the ISM. This result is not too surprising, for the fiducial TNG model sets the wind metal loading factor $\gamma_w = 0.4$ (Vogelsberger et al. 2013), indicating that the winds carry metals with a fraction of the metallicity of the ISM. However, as the winds reach the scale of the galaxy, they entrain additional metal mass, as evidenced by the fraction of metals outflowing consistently being greater than 0.4 (the grey dashed line in the center right panel).

In addition to calibrating outflow metal loadings, we also adjusted the metal inflow efficiencies to capture the metallicity of gas entering

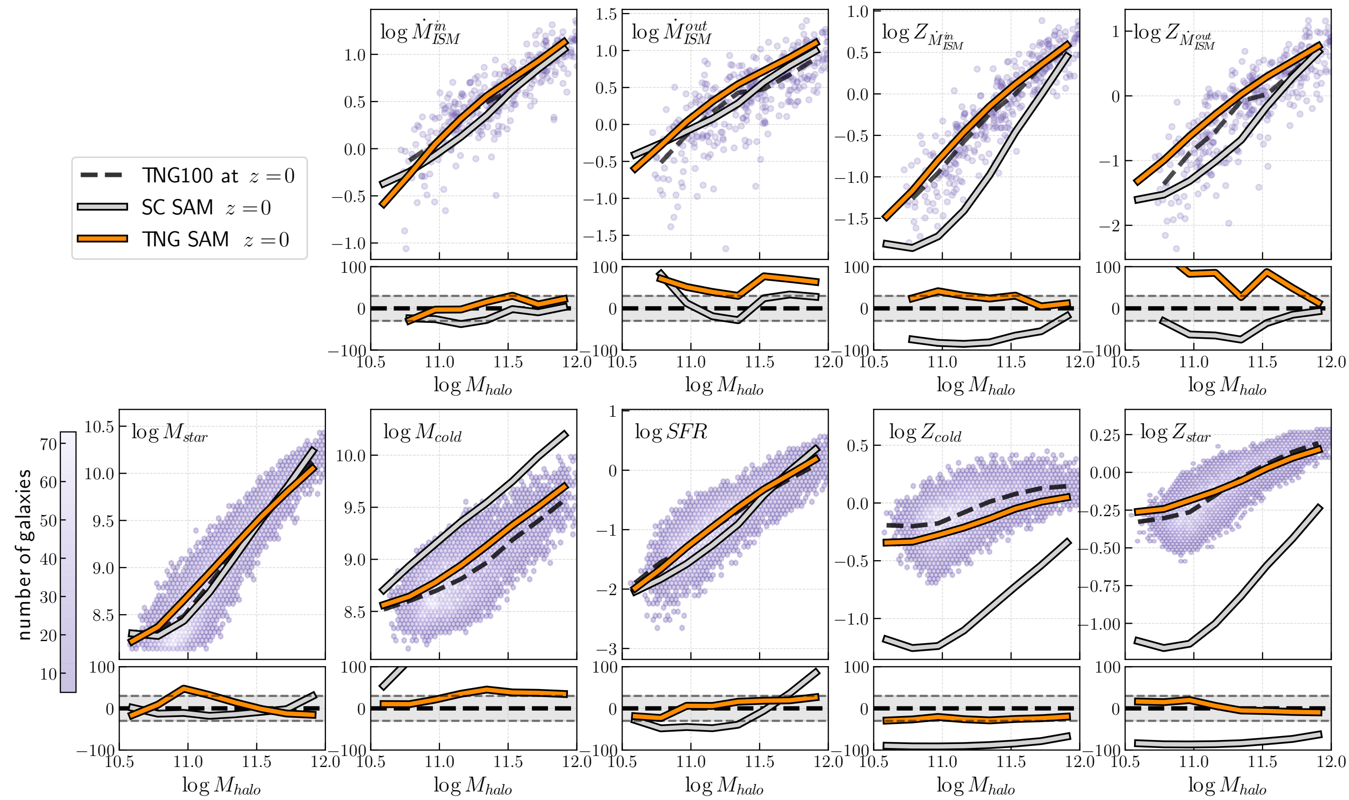

Figure 5. it agrees i promise just haven't updated the tng sam shown Comparison of baryon flow rates (top panels) and global galaxy properties (bottom panels) at the galactic scale for the TNG SAM (orange), SC SAM (gray), and TNG100 (purple). Each panel shows the median (50th percentile) predictions from the SAMs compared to the TNG100 population, represented by scatter points for the Cohen et al. sample and histograms for the full TNG100 dataset, with TNG100 medians indicated by dashed black lines. Residuals below each panel show the percentage difference between the median TNG100 population and the SAMs, with the shaded gray region marking deviations within ±30%. The SC SAM mostly lies outside 30% of TNG's median distribution, and generally differs by around 70%, with variations up to 200% in the worst cases (e.g., $\dot{M}_{\rm CGM,in}$). The recalibrated TNG SAM, now not only calibrated to match observations but also calibrated to emulate the underlying baryon cycle in TNG, greatly improves upon the SC SAM's predictions, and mostly agrees within 30% of TNG's median distribution.

the ISM and CGM from the CGM and IGM, respectively. For the ISM, we define $\zeta^{\rm in}_{ISM}$ as:

$$\zeta^{\rm in}_{ISM} = \frac{\dot{M}^{\rm in}_{\rm Z,ISM}}{\dot{M}^{\rm in}_{ISM} \cdot Z_{\rm ISM}}, \tag{17}$$

where $\dot{M}_{\rm Z,inISM}$ is the metal inflow rate into the ISM, $\dot{M}_{\rm inISM}$ is the total gas inflow rate, and $Z_{\rm CGM}$ is the metallicity of the CGM. For the CGM, since the SAM does not track the metallicity of the IGM, we define $\zeta^{\rm in} CGM$ as the fraction of metals entering the CGM compared to the total rate of gas flowing into the CGM:

$$\zeta^{\rm in} CGM = \frac{\dot{M}^{\rm in}_{\rm Z,CGM}}{\dot{M}^{\rm in}_{\rm CGM}}. \tag{18}$$

Notably, the top right panel of Figure 3 shows that, in TNG, the proportion of metals returning to the ISM significantly exceeds unity, the original assumption in the SC SAM. This indicates that the gas returning to the ISM is more metal-rich than the CGM, suggesting efficient recycling of expelled metals back into the ISM.

While neither the SAM nor TNG explicitly track the metallicity of the IGM, the non-zero value of $\zeta^{\rm in} CGM$ implies a non-negligible inflow of metals into the CGM. This suggests that a fraction of the metals ejected via feedback processes can escape the halo and subsequently be re-accreted, highlighting the importance of considering metal recycling on both galactic and halo scales.

Finally, we also increased the stellar yield from the fiducial value of 1.2 in the SC SAM to 2.0 to better match the aggregate stellar metallicity observed in TNG galaxies.

4 REPRODUCING TNG100'S RESULTS OVER 12 GYR

As discussed in Section 1, different gas and metal flow cycles, as modeled by hydrodynamical simulations and SAMs, can follow distinct processes yet still converge on similar global predictions for galaxies. The SC SAM and TNG100, for example, represent gas cycling processes differently, but still arrive at similar global outcomes, as shown in Gabrielpillai et al. 2022. The primary goal of the TNG SAM is not only to predict these global properties but also to accurately replicate the underlying gas and metal flow cycles observed in TNG, using the recalibrations discussed in Section 3. In this section, we assess how accurately the TNG SAM replicates the global gas and metal flow cycles as well as global properties at the scale of the galaxy and halo in TNG100, achieving accuracy within 30%. We also compare the TNG SAM to the fiducial SC SAM at $z = 0$, highlighting how the differences in how each SAM's galaxy formation model changes its predictions.

4.1 The Galaxy Scale

At the scale of the galaxy, we evaluate how well the TNG SAM replicates gas and metal flows at $z = 0$ among TNG100, the TNG

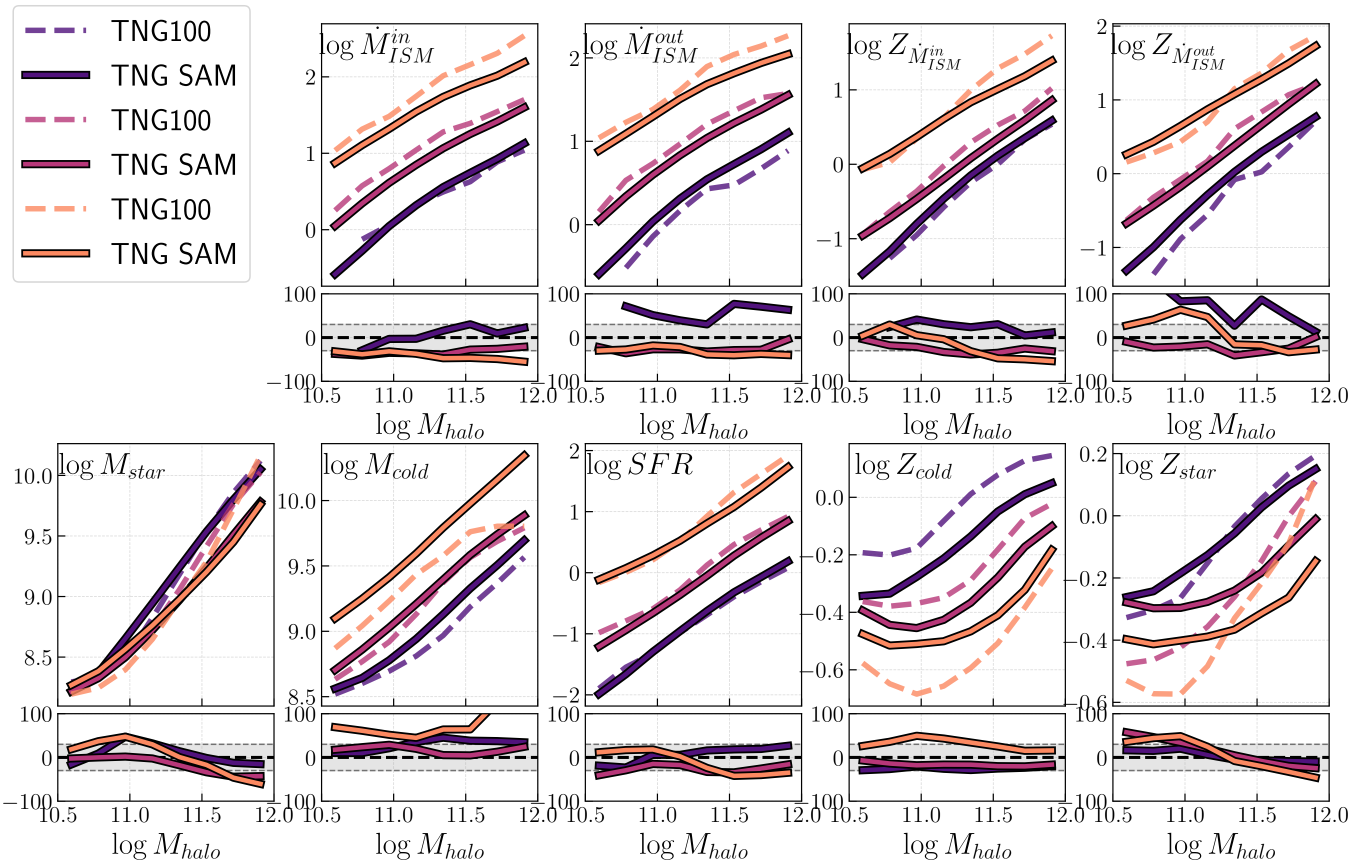

Figure 6. haven't updated the sam shown The time evolution of the same median galactic scale flow (top panels) and global properties shown in Figure 5 between the TNG SAM (solid lines) and TNG100 (dashed lines) at $z = 0.5, 2, 6$, with red, orange, and magenta lines representing each redshift, respectively. The TNG SAM closely replicates the gas flow rates in TNG, staying within 30% of TNG's median values. We observe similar agreement with the aggregate global galaxy properties as well.

SAM, and the fiducial SC SAM in the top panel of TNG Figure 5 compares the rates of gas and metal inflows and outflows at $z = 0$ among TNG100, the TNG SAM, and the fiducial SC SAM.

For the rate of gas inflow into the ISM (top left panel), the TNG SAM matches TNG100's inflow patterns, with a median difference of 16% across the entire $10.5 < \log M_{\rm halo} < 12$ mass range shown. The SC SAM shows $\sim$ 40% higher inflow rates than TNG across halo masses, likely due to its shorter cooling times. For gas outflows from the ISM (second panel from the left), the TNG SAM aligns with TNG100's more moderate outflow rates, achieving a median difference of 14%. In contrast, the SC SAM predicts 40% higher outflow rates, especially in high-mass halos, driven by its more efficient stellar feedback model. The TNG SAM also closely matches the behavior seen in TNG100 for metal inflows and outflows in the ISM (top right panels), achieving a median accuracy of 30% for inflows and 16% for outflows across halo masses. In contrast, the SC SAM predicts higher metal inflows at high halo masses and lower inflows at low masses, as well as higher metal outflows at higher halo masses, due to its simplified metal recycling model, discussed further in Section 5.1.5, leading to $\sim$ 80% differences.

The TNG SAM's ability to reproduce gas flows into and out of the galaxy within $\sim$ 30% of TNG's values translates into similarly good agreement with TNG for global galaxy properties. The lower panel of Figure 5 compares the distributions of global galaxy properties – stellar mass, cold gas mass , star formation rate and the metallicities of the stellar population and cold gas.

The TNG SAM closely matches the stellar mass predicted by TNG, reducing discrepancies to within 10% on average. The SC SAM, while differing in its treatment of gas accretion and star formation, still agrees with TNG's predictions within 30% across the mass range shown, demonstrating once again that different cycling processes can still produce the "correct" outcome for various galaxy and halo properties, likely due to similar calibrations. For cold gas mass (second row, left panel), the TNG SAM performs reasonably well, keeping most differences within 33%. The SC predicts cold gas masses $\sim$ 200% higher than TNG, but this is likely due to the different star formation models both use. The SC SAM forms stars from molecular hydrogen partitioned using the Bigiel et al. 2008 recipe, while TNG and the TNG SAM apply the Kennicutt-Schmidt relation. If we consider all cold gas as the sum of neutral and molecular hydrogen in the SC SAM, the discrepancy drops to around 80%. TNG's star formation rate (bottom left panel) shows excellent agreement with the TNG SAM, typically within 20%. The SC SAM generally predicts lower SFRs across the mass range, again likely due to its different star formation model.

Metallicities in the TNG SAM show impressive agreement with TNG compared to the fiducial SC SAM model. The SC SAM predicts stellar and cold gas metallicities $\sim$ 70% below the metallicities predicted by TNG, with TNG's predictions for stellar and cold gas metallicities better matching observations. In contrast, the TNG SAM closely follows TNG's predictions, with deviations under 20% for all properties.

To assess how well the TNG SAM's agreement with TNG at $z = 0$ holds as we travel back further in time, Figure 6 shows the same properties evaluated in Figure 5 now at $z = 0.5, 2$ and 6. For gas inflows into the ISM, the TNG SAM generally stays within 30%

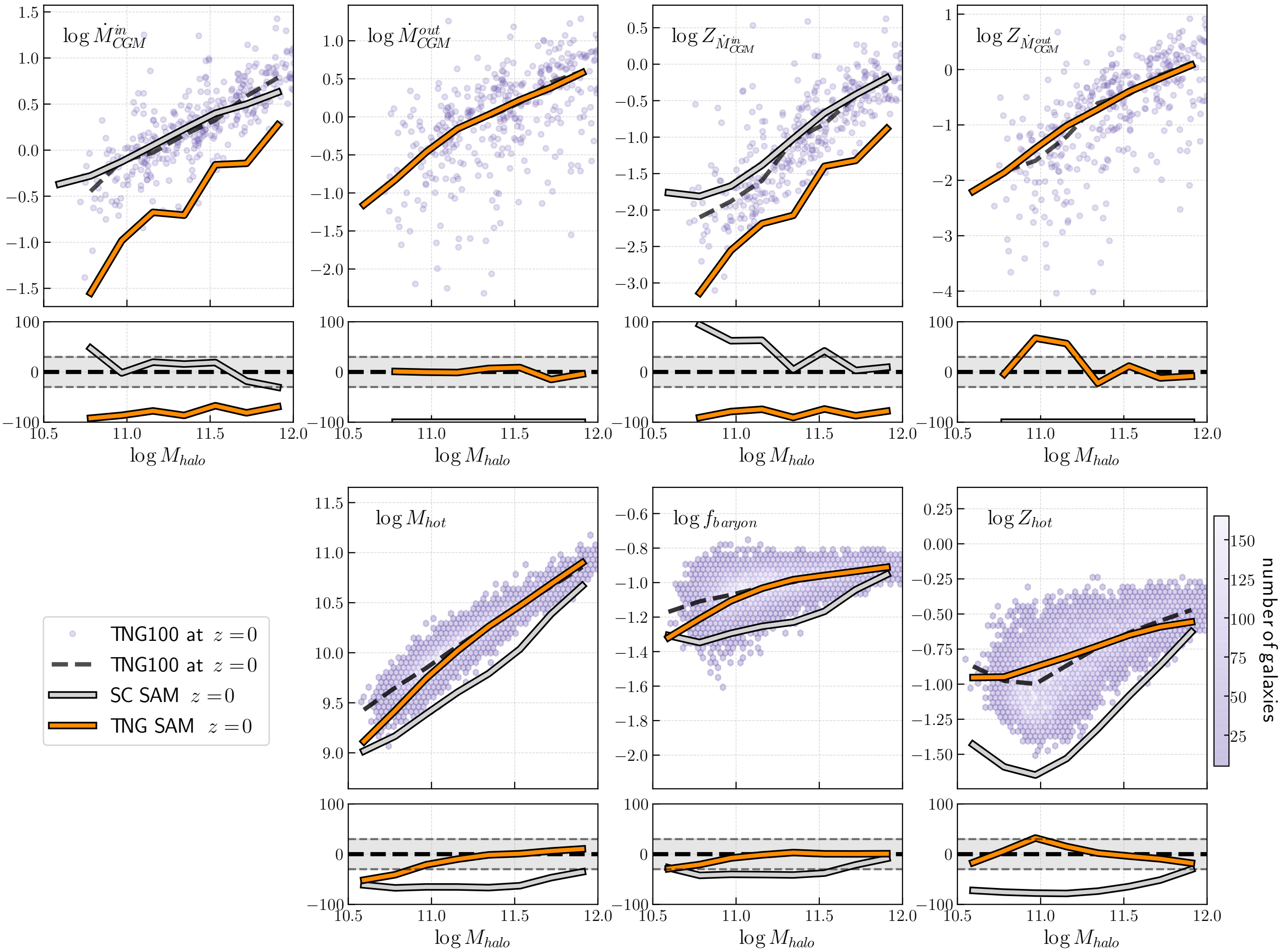

Figure 7. The same comparison done in Figure 5 now at the halo scale at $z = 0$.

of TNG, though differences increase to about 50% at lower halo masses, especially at earlier times. For gas outflows from the ISM, the TNG SAM performs well across all masses, with deviations as low as 16% at high masses. Metal inflows into the ISM show greater variability, with the TNG SAM tracking TNG's more gradual metal recycling processes, staying within 30-60% for intermediate to low halo masses. For metal outflows, the TNG SAM maintains consistency, with deviations under 30% at most masses.

For global properties, the TNG SAM consistently tracks TNG's stellar mass, cold gas mass, and star formation rate within 30% across time, with slightly larger deviations at earlier epochs. For example, the TNG SAM shows a maximum deviation of 80% for stellar mass at early times for higher-mass halos, but the median deviation stays within 13%. For the metal populations, the TNG SAM consistently provides good ($< 30\%$) agreement with TNG for the stellar and cold gas metallicities.

4.2 The Halo Scale

At the scale of the halo, we evaluate how well the TNG SAM replicates gas and metal flows at $z = 0$ among TNG100, the TNG SAM, and the fiducial SC SAM in the top panel of TNG Figure 7 compares the rates of gas and metal inflows and outflows at $z = 0$ among TNG100, the TNG SAM, and the fiducial SC SAM.

For gas and metal flows in the halo, the TNG SAM generally matches TNG's predictions within 30%. The SC SAM, using a more simplified model for gas accretion, tends to show higher gas inflow rates up to 60% higher than TNG across halo masses. In contrast, the TNG SAM better captures the detailed inflow behavior observed in TNG, staying mostly within 16%. For metal inflows, the SC SAM predicts higher rates due to more efficient recycling, while the TNG SAM aligns more closely with TNG's more gradual metal flows, maintaining accuracy within 30% across the mass range. One of the most notable changes in the TNG SAM is the explicit inclusion of gas and metal expulsion from the CGM to the ejected reservoir, a channel not included in the SC SAM. The TNG SAM's gas and metal outflow rates agree with TNG's within $\sim 18\%$, and 30%, respectively. For gas outflows from the CGM, the TNG SAM remains within 30% across all mass bins, matching TNG closely.

As shown at the galaxy scale in Section 4.1, the TNG SAM's ability to reproduce gas flows in the CGM within $\sim 30\%$ of TNG's values translates into similarly good agreement with TNG for global halo properties. The lower panel of Figure 7 compares the distributions of global halo properties – hot gas mass, overall baryon fraction and the metallicity of the hot gas reservoir across TNG100, the SC SAM, and the TNG SAM.

The TNG SAM shows excellent agreement with TNG on the mass of the hot halo, keeping deviations generally within 20% across the halo mass range. The SC SAM, however, predicts a hot gas mass generally 60% lower than TNG's values. For the overall baryon fraction,

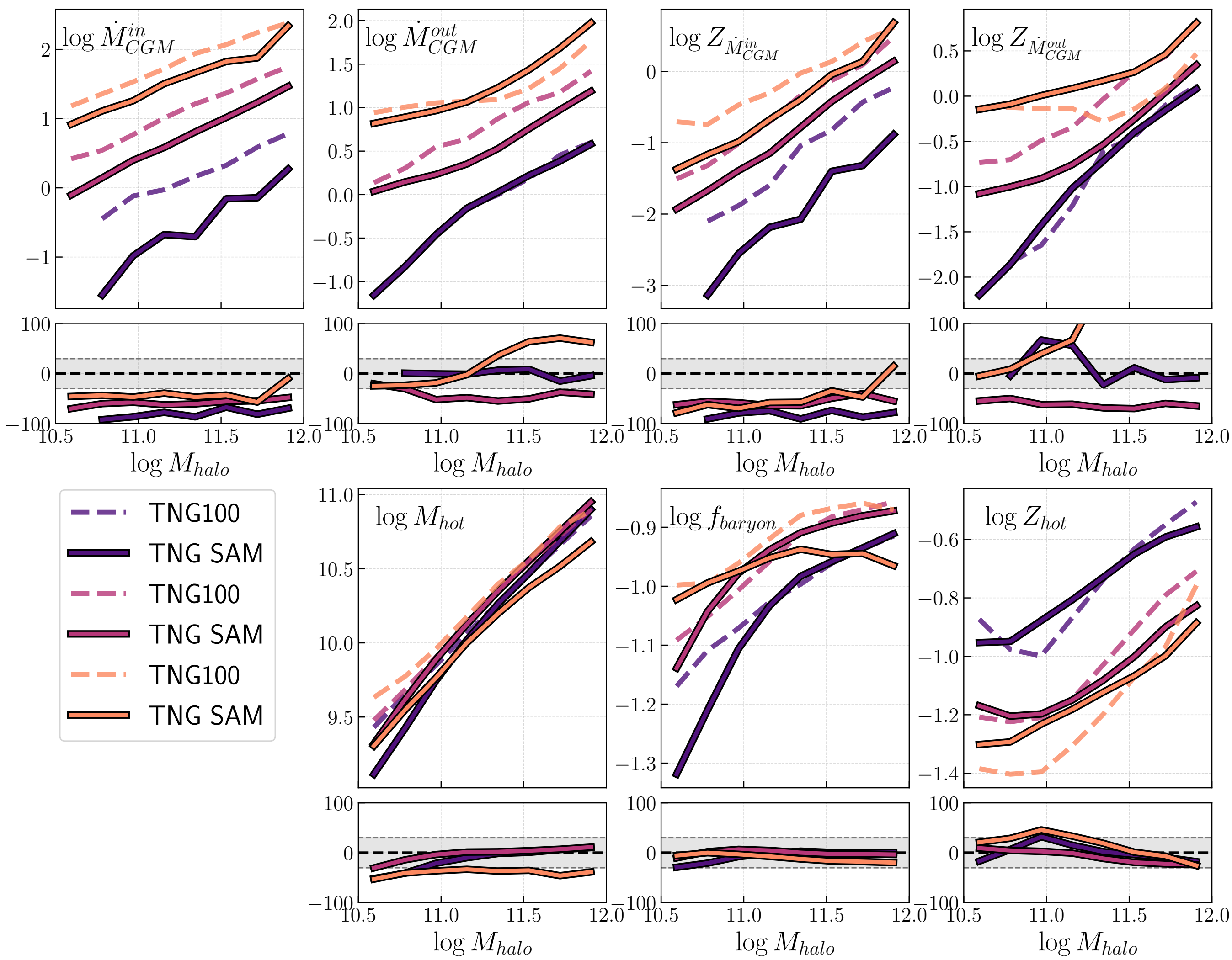

Figure 8. The time evolution of the same median halo scale flow (top panels) and global properties shown in Figure 7 between the TNG SAM (solid lines) and TNG100 (dashed lines) at z = 0.5, 2, 6, with each redshift corresponding to a different color.

the TNG SAM again generally matches TNG within 12% accuracy across the halo mass range. The SC SAM generally predicts ∼ 40% lower baryon fraction across low - intermediate halo masses, unsurprising given its underprediction of the hot halo gas mass. As shown at the galaxy scale, the TNG SAM continues to show impressive agreement with TNG for the metallicity of the hot gas reservoir compared to the fiducial SC SAM model. The SC SAM predicts hot gas metallicities ∼ 70% below the metallicities predicted by TNG. In contrast, the TNG SAM closely follows TNG's predictions within 20%.

In Figure 8, we examine how the TNG SAM's agreement with TNG holds over time. For gas and metal inflows and outflows into/from the CGM, the TNG SAM remains within 30% across time, matching TNG closely. For the global halo properties, the TNG SAM's predictions for the overall baryon fraction and hot gas mass remain well-aligned with TNG across time, within 30% accuracy. For the metal population, the TNG SAM consistently provides good (< 30%) agreement with TNG for the hot gas metallicities.

5 DISCUSSION

5.1 Why do the SAM and TNG Agree?

The TNG SAM's ability to reproduce many galaxy and halo properties in TNG mostly within 10–30% highlights the adaptability of semi-analytic models, and also demonstrates the effectiveness of recalibrating SAMs using the physical insights gained from hydrodynamical simulations. Below, we discuss the key physical modifications made to the TNG SAM and discuss their impact on the agreement described in Section 4. Figure 9 illustrates the performance of the TNG SAM both before and after these adjustments at z = 0, summarizing the contributions of each modification to the model's accuracy.

5.1.1 Efficient Halo (Re-)accretion: Strong Gas Recycling and Weak Preventive Feedback

A key factor driving the success of the TNG SAM in replicating TNG's baryon cycle is $f_{\rm in,CGM}$, which governs the efficiency of gas accretion into halos. As shown in Figure 10, $f_{\rm in,CGM}$ in TNG frequently hovers around or exceeds unity, especially at lower redshifts. This contrasts with the lower $f_{\rm in,CGM}$ values observed in other hydrodynamical simulations such as FIRE (Pandya et al. 2020; Pandya

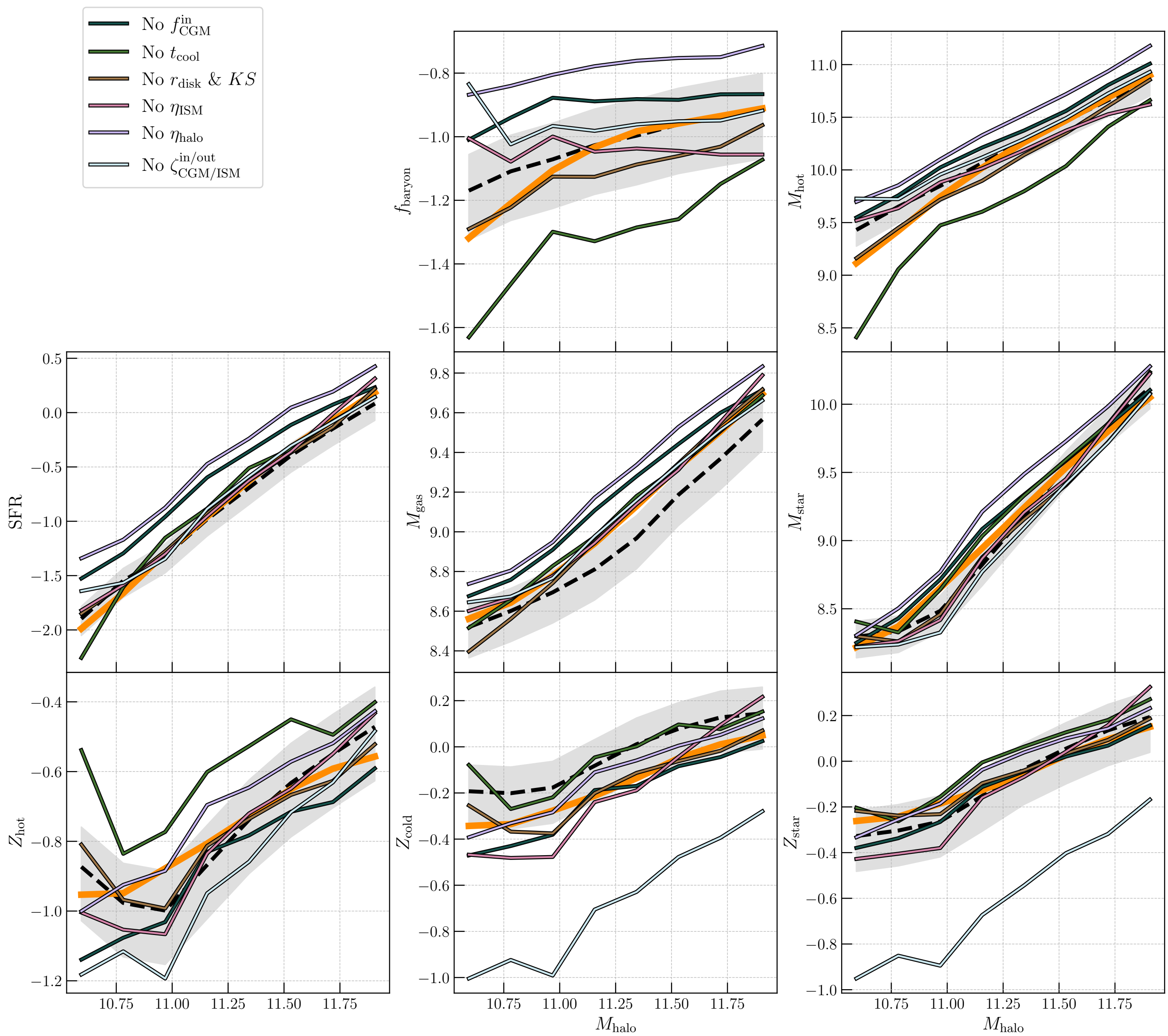

Figure 9. tweaking colorsTo evaluate the importance of each calibration made to the TNG SAM, we show how reverting each parameter to its original SC SAM formulation impacts the TNG SAM's ability to reproduce TNG's global results at the galaxy and halos scale at $z = 0$. The 50th percentile of the original TNG SAM is shown as a solid orange line, while TNG100 median distribution as a dashed black line. The 30% agreement range is shaded in gray. Each additional solid line corresponds to the TNG SAM with a specific parameter reverted to the original SC SAM recipe, demonstrating the impact of each calibration on the global properties shown in each panel.

2021) and EAGLE (Mitchell et al. 2020; Mitchell & Schaye 2022; Wright et al. 2020)[1]. In FIRE and EAGLE, $f_{\rm in,CGM}$ typically falls below unity due to stronger "preventive" feedback, which heats gas in the IGM and limits accretion onto halos. In TNG, however, gas recycling likely plays a dominant role, allowing ejected gas to efficiently re-enter the halo and overcome preventive feedback mechanisms that might otherwise inhibit this process.

This efficient re-accretion process likely explains why $f_{\rm in,CGM}$ remains elevated in TNG, even when gas is expelled by stellar and/or AGN feedback. For low-mass halos ($10.5 < \log M_{\rm halo} < 11$), stellar feedback likely drives the majority of the ejective feedback. However, for the intermediate ($11 < \log M_{\rm halo} < 11.5$) and high-mass ($11.5 < \log M_{\rm halo} < 12$) halos, AGN feedback likely becomes increasingly important in contributing to the amount of gas ejected and eventually re-accreted. CIP note that for these halos, the number of galaxies dominated by AGN vs supernovae feedback is roughly balanced.

In the TNG SAM, $f_{\rm in,CGM}$ replaces the fixed gas return fraction ($f_{\rm return} = 0.1$) used in the SC SAM. Most SAMs use a similar uncertain static fraction (e.g. 0.64 in GALFORM, 1.0 in L-galaxies) to model re-accretion across all halo masses and redshifts, which oversimplifies the dynamic accretion processes observed in hydrodynamical simulations. Without $f_{\rm in,CGM}$, the TNG SAM overpredicts the hot gas mass ($M_{\rm hot}$) by 20%, resulting in increases in cold gas and stellar mass by 25-35%, and inflating the overall baryon fraction by nearly 40%. The variability of $f_{\rm in,CGM}$ in the TNG SAM reflects the

[1] To compare all three hydrodynamical simulations in a consistent manner, we take the values reported in Pandya et al. (2021) for FIRE and Wright et al. (2024) for EAGLE, as both studies extract flow rates using an Eulerian approach, as Cohen et al. (in preparation) has done for TNG

varying gas recycling efficiency in TNG, capturing the more complex accretion behavior across different halo masses.

Despite the effectiveness of $f_{\rm in,CGM}$ in the TNG SAM, a significant limitation lies in the uncertainty regarding the precise nature of gas recycling in TNG. The mesh-based approach of TNG prevents detailed tracking of whether re-accreted gas is pristine or recycled, unlike particle-based simulations like EAGLE, where gas flows can be tracked more explicitly. In EAGLE, for instance, Mitchell & Schaye (2022) found that the halo recycling efficiency increases monotonically with halo mass and redshift. If such tagging were possible in TNG, it would provide valuable insights into whether preventive feedback still plays a role in first-time gas accretion in low-mass halos, although recycling is clearly the dominant process once it begins.

Looking ahead, the next generation of SAMs would greatly benefit from incorporating more flexible and physically motivated recycling models, informed by the explicit tracking of gas flows observed in hydrodynamical simulations. While the $f_{\rm in,CGM}$ parameter represents an important step in replacing the *ad hoc* static recycling fractions used in most SAMs, further refinement—such as directly modeling recycling efficiency as it evolves with halo mass and redshift—would be invaluable. For example, the latest version of SAGE (Croton et al. 2016) adjusts the reincorporation rate to increase for massive halos, motivated by fitting the SAM to multiple simulations, and we now see also holds in EAGLE. However, we find that this approach does not translate well to the TNG SAM. Therefore, ensuring that these models remain flexible enough to account for a range of recycling efficiencies is essential. Such improvements will ultimately enhance our understanding of how preventive feedback, re-accretion, and recycling processes shape galaxy evolution, especially as simulations expand to larger volumes.

5.1.2 *Revised Cooling Model: Limitations of the Cold-Mode vs. Hot-Mode Dichotomy*

Another significant improvement to the TNG SAM came from revising the cooling model for the hot halo gas onto the central galaxy. The overwhelming majority of SAMs published in the literature (e.g., Galacticus Benson 2012, Shark Lagos et al. 2018, GAEA Hirschmann et al. 2016, Morgana Monaco et al. 2007) classify gas accretion as either "cold-mode" or "hot-mode" based on the cooling radius. In these models, radiative cooling is governed by well-established processes such as collisional excitation, ionization, recombination, and bremsstrahlung, with the assumption that the hot gas is shock-heated to the virial temperature of the host halo and that chemical abundances are well-mixed throughout the gas. As cooling depends on the gas density and metallicity, denser gas at the center of the halo cools faster than outer gas, resulting in an inside-out cooling pattern. While this simplified approach captures the basic mechanisms of gas cooling, it has been shown to lead to systematic discrepancies when compared to cosmological hydrodynamic simulations, with SAMs underpredicting gas accretion rates in low-mass halos but overpredicting them in massive halos (Lu et al. 2011).

In TNG, we find the traditional cooling model has the opposite trend for low-mass halos. The left panels of Figure 11 shows that cooling times in TNG often exceed the expected timescales for both cold- and hot-mode accretion. Even in halos where the cooling radius exceeds the virial radius (the cold-mode regime), the cooling time frequently surpasses the dynamical time (dashed line). If cooling were dominated by these rapid, cold-mode flows, as assumed in some SAMs (e.g., GalICS; Cattaneo et al. 2017), we would expect significantly shorter cooling times and higher accretion rates than those observed in TNG. However, the TNG model accounts for additional local factors such as the gas density, temperature, element-based metal line cooling, and radiation field from the UV background and nearby AGN, which modulate the radiative cooling rate. This results in a more gradual cooling of the hot halo gas, contrasting with the rapid collapse predicted by cold-mode flows and the delayed cooling expected from hot-mode accretion. Although identifying the exact refinements in TNG's radiative cooling model that lead to disagreement with SAMs is beyond the scope of this paper, such an investigation could provide valuable insights for refining SAMs in the future.

Interestingly, this trend persists outside of TNG. The right panel of Figure 11 compares the cooling times in TNG with the cooling times reported in FIRE, adopted from Figure 4.22 of Pandya (2021), with both simulations predicting cooling times longer than the dynamical time at low redshift. In both TNG and FIRE, radiative cooling is implemented using similar physical processes, including collisional excitation, ionization, recombination, and metal-line cooling driven by local gas properties. However, the treatment of feedback differs substantially. The FIRE simulations employ a highly resolved, explicit treatment of stellar feedback, capturing the localized and stochastic nature of supernovae, stellar winds, and radiation pressure. On the other hand, TNG utilizes a more parameterized approach with sub-grid models that distribute feedback energy and momentum over larger scales. Despite these differences in feedback implementation, both simulations produce similar results in terms of cooling times, even in halos traditionally classified as 'cold mode.' This lends further credence to the idea that the traditional cooling model used in SAMs, which simplifies the interaction of radiative cooling, feedback, and turbulence, may miss key aspects of gas dynamics in more realistic galaxy environments.

To address this shortcoming, we revised the TNG SAM's cooling model to align with the cooling times in TNG. This revision leads to significant improvements in the SAM's predictions of halo-scale properties compared to the traditional cooling model, as illustrated in the top row of Figure 9. The traditional model, due to its fast cooling times, consistently underpredicts the mass of the hot halo by $\sim 60\%$, leading to elevated gas masses in the ISM. his revision highlights the importance of adopting more physically detailed cooling models in SAMs to better replicate the complex gas cooling processes observed in hydrodynamical simulations like TNG and FIRE.

A potential way to reconcile these approaches would be to account for the flow of energy in the SAM as well. Pandya et al. 2023; Carr et al. 2023; Voit et al. 2024a,b found introducing energy-tracking ordinary differential equations coupling the feedback energy to the CGM was needed to increase the cooling time to match FIRE-2 halos.

work this in: why we needed to introduce the Edot ODE's in Pandya+23 (and Carr+23/Voit+24a/Voit+24b) to couple feedback energy to the CGM to increase its cooling time

5.1.3 *KS Relations Facilitates Star Formation Agreement*

Despite the fundamental difference in spatial scales at which the KS relation is applied in TNG–locally at the scale of $10^6\ M_\odot$gas cells–and in the TNG SAM–globally across the entire galaxy–the TNG SAM successfully reproduces the global KS relation observed in TNG, leading to good agreement for all mass reservoirs in the ISM, specifically cold gas mass and stellar mass. This result is not particularly surprising, as the star formation law in TNG was explicitly calibrated to match the local, spatially resolved KS relation observed in nearby galaxies (Springel & Hernquist 2003). Although projecting quantities onto surface densities can slightly affect the slope of the

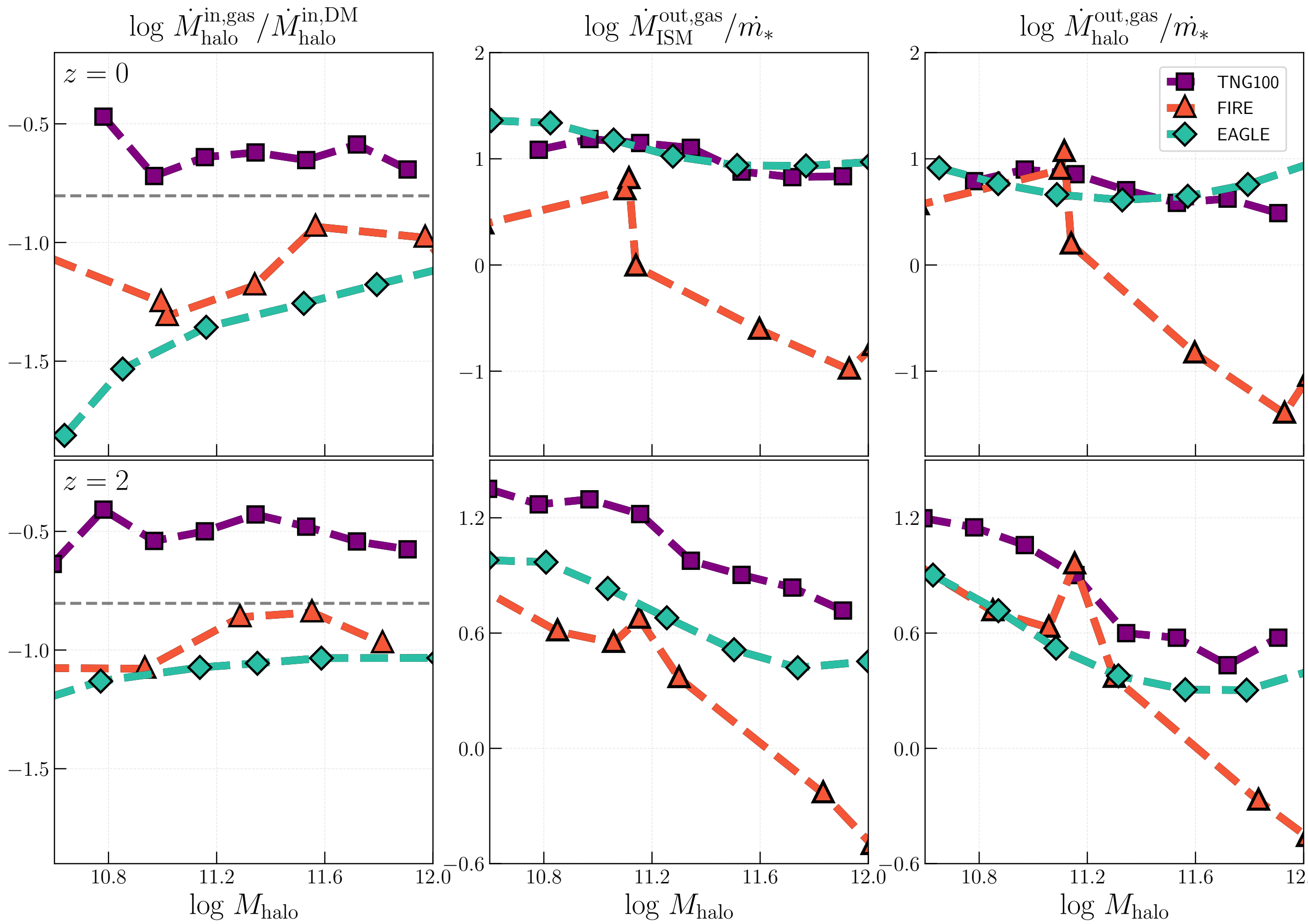

Figure 10. Comparison of the gas (re-)accretion efficiency parameter $f_{\rm in,CGM}$ as a function of halo mass ($M_{\rm halo}$) at $z = 0$ (left) and $z = 2$ (right) across multiple hydrodynamical simulations: TNG100 (purple squares), FIRE (orange triangles), and EAGLE (green diamonds). In TNG100, $f_{\rm in,CGM}$ often exceeds unity. This contrasts with lower values of $f_{\rm in,CGM}$ observed in FIRE and EAGLE, particularly in low-mass halos, where preventive feedback processes limit gas accretion. The higher inflow rates in TNG100 suggest that efficient gas recycling in TNG overcomes the effects of preventive feedback. eta comparison probably not needed, just refer to (Wright et al. 2024)

KS relation, the assumption of nearly constant scale heights ensures that the relationship between 3D densities and surface densities is preserved, as demonstrated by Diemer et al. (2018), who showed that the KS law also remains consistent globally in TNG. Furthermore, observational studies (e.g., Kumari et al. 2020), have shown that the KS relation holds consistently across a wide range of scales, from macroscopic regions within galaxy disks (hundreds of parsecs) to the entire galaxy. Detailed numerical simulations, too, have demonstrated that the KS law remains robust from global to local scales (e.g., Kravtsov 2003; Li & Nakamura 2006). As a result, the agreement between TNG and the TNG SAM is likely a reflection of the broader robustness of the KS relation.

However, it is important to note that while the global total gas KS relation is reproduced well in both TNG and the TNG SAM, the same cannot necessarily be said for the molecular KS relation. Observational studies (e.g., Bigiel et al. 2008) have shown a linear molecular gas Schmidt relation, in contrast to the super-linear total gas relation seen in entire galaxies. In TNG, Diemer et al. 2018 show that this molecular KS relation is not strictly obeyed, with the simulation results showing a superlinear relation with a slope of 1.5. Since TNG does not explicitly output molecular gas, direct comparisons between molecular gas predictions in TNG and the SAM remain difficult. Given this limitation, the total gas KS relation serves as the most reliable metric for comparing the two models and is successful.

We note, however, that the success of the KS relation is highly dependent on consistently modeling the disk sizes in TNG and the TNG SAM. The majority of the SAMs, including the SC SAM, determine disk sizes through angular momentum conservation under the assumption of an exponential disk. While this method achieves reasonably good agreement with observed radial disk sizes as a function of stellar mass up to $z \sim 2$ in the SC SAM (Somerville et al. 2008b), it does not align with observations as well as TNG's predictions (Genel et al. 2018). Particularly, the SAM tends to underestimate disk sizes for lower-mass halos and at higher redshifts (see Karmakar et al. (2023) Figure 2).

These results suggest that SAMs utilizing surface density-based star formation models, like the Kennicutt-Schmidt relation, can still provide robust predictions for ISM properties, even when applied at the global scale of the galaxy rather than locally. However, they also underscore the importance of accurately modeling disk sizes, as mismatches can lead to discrepancies in gas and stellar mass predictions. Therefore, achieving reliable predictions for cold gas and stellar masses in galaxies will require developing more physically motivated models for estimating disk sizes in SAMs.

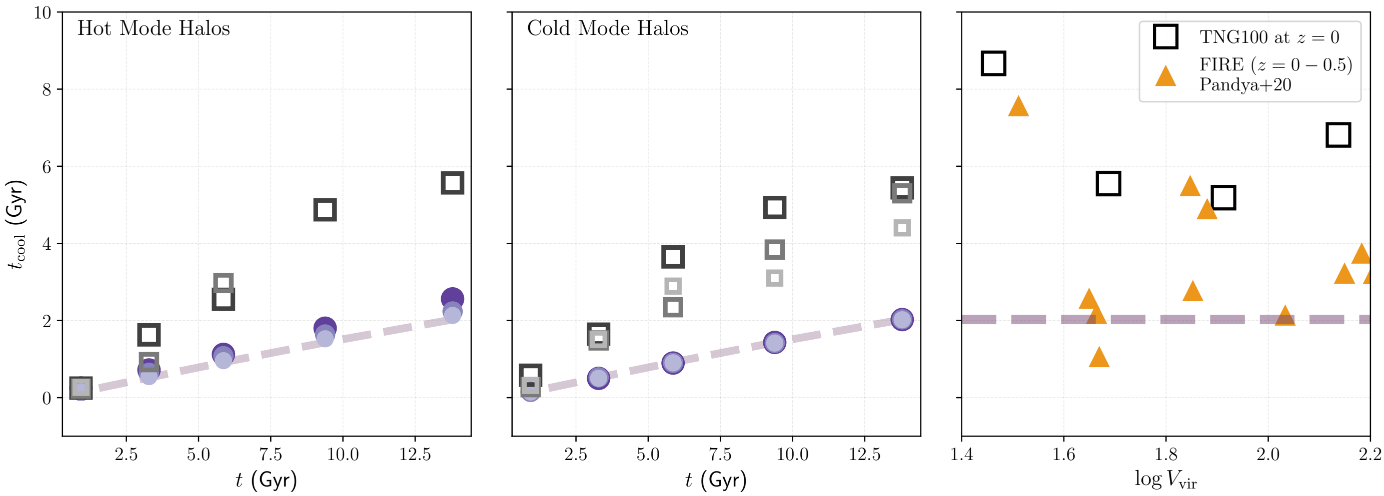

Figure 11. The left two panels present the time evolution of cooling times ($t_{\rm cool}$) for hot-mode halos ($r_{cool} < r_{\rm vir}$; top panel) and cold-mode halos ($r_{cool} > r_{\rm vir}$; bottom panel) in TNG (squares) and the SC SAM (circles). The dashed purple line represents the dynamical time for a $10^{11}\ M_{\odot}$halo. In TNG, the cooling time consistently remains far above the dynamical time for both cold-mode and hot-mode halos, indicating that the traditional binary classification of gas accretion used in SAMs does not adequately capture the complexity of the cooling processes observed in TNG. The right panel compares the cooling times ($t_{\rm cool}$) as a function of virial velocity ($V_{\rm vir}$) in SC SAM (purple circles), TNG100 (black squares), and FIRE (orange triangles).Data from FIRE simulations are taken from Pandya (2021), and plotted for $z = 0 - 0.5$. Despite the differing numerical approaches to modeling galaxy formation, both TNG and FIRE on average predict cooling times significantly longer than the dynamical time (dashed line).

5.1.4 *ISM and Halo-Scale Outflows: Critical for Accurate Hot and Cold Gas Masses*

While galaxy-scale outflows are well-established as incredibly important regulators of galaxy evolution in numerical simulations, recent studies have underscored the importance of outflows at the halo scale as well (Wright et al. 2024; Pandya et al. 2021; Mitchell et al. 2020). Consistent with these findings, we observe that both galaxy and halo-scale outflows are essential for accurately modeling the gas content in the TNG SAM. Specifically, the masses of the ISM and CGM are highly sensitive to the strengths of the outflow efficiency parameters $\eta_{\rm ISM}$ and $\eta_{\rm halo}$, as shown in the top and middle columns of Figure 9.

Incorporating TNG's galactic winds model into the TNG SAM, which explicitly links the strength of the winds to the metallicity of the cold gas, significantly improved the TNG SAM's ability to reproduce the observed galaxy scale outflow rates in TNG. This refinement, despite the additional complexity introduced by the metallicity dependence, proved crucial as the original stellar feedback model in the SC SAM tends to overestimate the strength of galaxy outflows by 30% (see Figures 5 and 6). This leads to the SC SAM overestimating the gas expelled, thus increasing $M_{\rm hot}$and $f_{\rm baryon}$. By contrast, the more physically motivated TNG approach, where feedback is modulated by local metallicity, provides a less extreme treatment of how outflows behave within the galaxy.

The most critical update to the TNG SAM's feedback model, however, was the explicit inclusion of halo-scale outflows, a process indirectly present in the SC SAM, and directly included in few other traditional SAMs (e.g. GALFORM SAMs Bower et al. (2012); Lacey et al. (2016)). Unlike the SC SAM, which only allowed gas to be ejected directly from the ISM into the ejected reservoir, the TNG SAM introduces a more realistic channel for these outflows. Gas first leaves the ISM and enters the CGM, where it continues to interact with the hot halo. From there, a significant portion of this gas can be further expelled into the ejected reservoir/IGM, forming the CGM-to-IGM outflow channel. This two-step process provides a more realistic depiction of how gas is cycled and expelled, as opposed to the simplified ISM-to-ejected reservoir flow used in many traditional SAMs. The fifth column of Figure 9 shows that neglecting halo-scale outflows leads to substantial overpredictions of $M_{\rm hot}$and $f_{\rm baryon}$by up to 80%. The effects propagate to the ISM, where $M_{\rm cold}$, SFR, and $M_{\rm star}$are overestimated by as much as 100%, 180%, and 60%, respectively.

5.1.5 *Metal Cycling Efficiencies Improve Metallicity Predictions*

Incorporating metallicity-weighted mass-loading factors significantly improved the TNG SAM's ability to replicate the evolution of metallicities in cold gas, stars, and hot halo gas in TNG100. Without these refinements, the TNG SAM underpredicts cold gas and stellar metallicities by up to $\sim$ 70%, as shown in the last row of Figure 9. While the metallicity of the CGM is less affected, discrepancies of up to 30% remain. By introducing metal cycling efficiencies, the TNG SAM reduces these discrepancies to within 15%, bringing its predictions into close alignment with TNG.

This success is particularly striking given that the TNG SAM employs an instantaneous recycling model, which assumes metals produced by stars are immediately mixed into the surrounding gas. This simplification omits the more realistic time delays in metal transport and mixing processes observed in TNG. Despite these limitations, the introduction of metallicity-weighted mass-loading factors compensates for the model's lack of detail, allowing the TNG SAM to better track metal flows between the ISM, CGM, and IGM.

Most SAMs in the literature also use similar instantaneous recycling models for metal production, although some models (e.g. GAEA) attempt to modify it by accounting for the lifetimes of different stellar populations. The overwhelming majority of these models, however, like the Santa Cruz SAM, also assume that metals are exchanged between the different baryonic reservoirs in proportion to the exchange of gas mass from each component. Few SAMs, such as SAG (Collacchioni et al. 2018) and GALFORM (Lagos et al. 2013), have experimented with incorporating metal loadings in a similar manner to the TNG SAM. However, these models found little impact on reproducing the observed stellar mass-metallicity relation, likely because their supernova feedback models are not tied to the metallicity of the gas. In contrast, the TNG SAM, mimicking the TNG model, explicitly ties feedback strength to gas metallicity, an approach also found to be critical in high-resolution zoom-in simulations of the ISM like TIGRESS (Kim et al. 2020b,a) and FIRE (Hopkins et al. 2018, 2023).

If future generations of SAMs aim to model feedback in a more physically motivated manner, similar to the aforementioned hydrodynamical simulations, incorporating metallicity-weighted feedback models and corresponding metal loadings will likely become necessary. As demonstrated in the TNG SAM, this approach can help address some of the shortcomings of the instantaneous recycling model and lead to more accurate predictions of metal abundances in galaxies and their surrounding gas reservoirs.

5.2 Limitations and Future Directions

Although Section 4 shows that the median galaxy population produced by the TNG SAM agrees quite well with TNG given the physical updates made, there are still several limitations to our approach, discussed below.

5.2.1 Modeling Individual Galaxies with Median-Based Calibrations

The TNG SAM is calibrated using median relations that reflect the aggregate behavior of galaxies within TNG, rather than customizing the model for individual galaxies. To test how well the TNG SAM's median-based calibrations replicate the detailed growth histories of individual galaxies observed in TNG, we systematically match identical subhalos from TNG and the SAM to conduct a direct, object-by-object comparison.

Figure 12 shows that although the median galaxy population in the TNG SAM lies mostly within 30% of the median TNG population, this spread widens significantly when we compare the galaxies on a halo by halo basis. We find about 50% of matched galaxies priedct accurate global galaxy properties to within 5%. The next 20% and next 5% are accurate to within 30% and within 60%, respectively. the remaining 25% of galaxies, however, vary widely, from within 60-200%.

Although it's not perfect, it's still very promising.

5.2.2 TNG100 DMO vs Hydrodynamical Simulations

A significant limitation to our approach arises from running the TNG SAM on the TNG100-1-DMO simulation while comparing results to the hydrodynamical TNG100-1 simulations. As noted in Section 2.4, the halo masses in the TNG100-1-DM and TNG100-1 simulations differ by up to 20% for low halo masses at $z = 0$. This discrepancy stems from the inclusion of baryonic processes in the hydrodynamical simulation, and varies inconsistently across redshift.

This variation has significant implications for the TNG SAM, particularly in how the model calculates the rate of gas accretion. The SAM derives the rate of gas accretion by finite differencing the halo masses reported by the DMO simulation. The mismatch between halo masses in the N-body and hydrodynamical simulations affects how well we can model parameters like $f_{\rm in,CGM}$, which governs the growth of the hot halo, which in turn regulates the build up of cold gas and stars in the ISM. Due to this discrepancy, directly tuning $f_{\rm in,CGM}$in the SAM to match the hydrodynamical simulation was not possible. Instead, we inferred the correct value of $f_{\rm in,CGM}$by attempting to match the rate of gas entering the CGM in TNG. This ultimately limits how well the TNG SAM can reproduce TNG's results.

5.2.3 Sample Size, Resolution and Snapshot Spacing

The TNG SAM's ability to reproduce TNG100's results is also constrained by the halo mass resolution and temporal resolution of the sample used for calibration. Although we consider a halo well-resolved if it comprises over 100 cells ($\log M_{\rm halo} > 10.5$), the measurements used to derive the efficiencies computed for the TNG SAM are extracted from thin shells within each halo. These thin shells, particularly for lower mass halos around $10^{10} M_{\odot}$, often contain far fewer resolution elements, leading to noisy estimates of the efficiencies and potential artifacts in the SAM's predictions at low halo masses, where the most significant discrepancies tend to occur. Moreover, halos modeled at $z = 0$evolved from even smaller halos earlier in the universe's history, making it difficult to derive accurate relations that capture the evolution of lower-mass halos.

Additionally, at higher redshift, the number of available merger trees diminishes, and galaxies become less resolved due to their decreasing sizes. This reduces the accuracy of the accretion rates derived from simple finite differencing. As a result, we have limited our analysis to $z = 6$, beyond which the reliability of the data steadily decreases.

The temporal resolution of the simulation data, determined by the snapshot spacing, also impacts the TNG SAM's accuracy. To quantify the impact, we compared the TNG SAM calibrated using all available snapshots of TNG flow sample to a version calibrated using only a subset of snapshots at $z = 0, 2, 4, 6$. Figure insert shows that although the TNG SAM's predictions remain largely unchanged for $M_{\rm hot}$, using coarser snapshot spacing leads to deviations of up to insetr percent from the finely spaced TNG SAM for $M_{\rm cold}$, $M_{\rm star}$, and metallicities currently, I'm finding things look good for the redshifts not tuned. what matters is a good mass range sample.. Although using more coarse snapshot spacing still produces general agreement, it suggests that a finer temporal resolution, if available, could further improve the TNG SAM's agreement with TNG100. Deriving these measurements for a wider redshift range, however, is incredibly computationally expensive, and contrary to our goal of developing flexible, computationally efficient SAMs.

add how many galaxies are needed to reproduce the TNG SAM. So far, I've selected 100 galaxies at random in the sample and still get similar results (accuracy within $\sim$ 50%. Cool! the most extensive observational surveys have about 600 galaxies (e.g. CALIFA) spatially resolved ones (e.g. PHANGS 90). Getting the TNG SAM close with 100 spatially resolved galaxies at each snapshot would be promising for observers, showing a well constrained sample can refine feedback prescriptions used in sims (though even more uncertain given we know the definitive answer and they don't)!

5.2.4 Future Directions

The TNG SAM, though successful in reproducing TNG100's baryon cycle and scaling relations for a limited halo mass range (10.5 > log $M_{\rm halo}$< 12), has several limitations, as discussed above. Expanding the analysis to galaxies in the TNG50 simulations, which resolves halos down to 10^8 $M_{\odot}$, would likely yield even more significant insights into the baryon cycle in lower-mass halos. Although TNG100

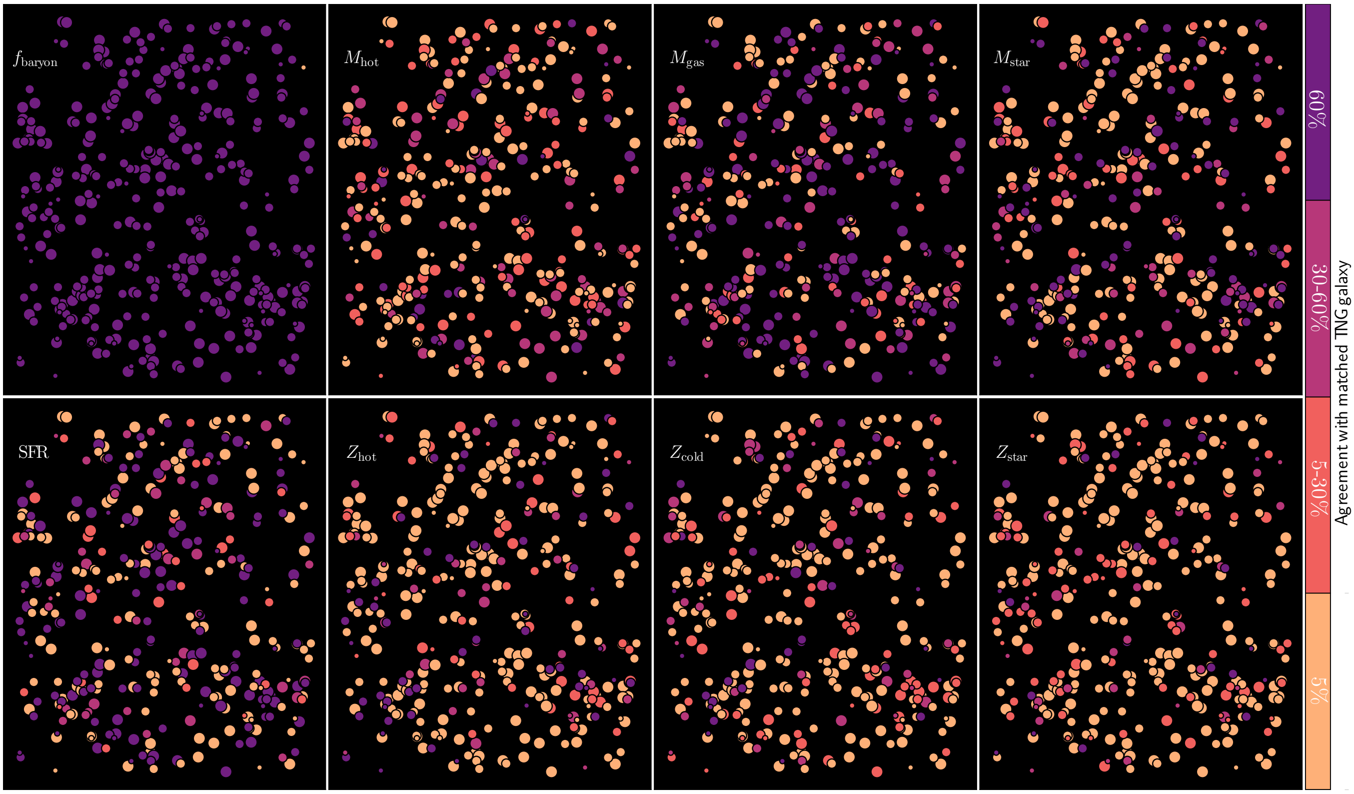

Figure 12. havent updated samSpatial distribution of galaxies in TNG100 at $z = 0$, plotted in physical space and matched halo-by-halo between the TNG SAM and TNG100. Each panel represents a specific property, including halo mass ($M_{\rm halo}$), hot gas mass ($M_{\rm hot}$), cold gas mass ($M_{\rm cold}$), stellar mass ($M_{\star}$), star formation rate (SFR), and the metallicities of cold gas ($Z_{\rm cold}$), hot gas ($Z_{\rm hot}$), and stars ($Z_{\rm star}$). The color of each point indicates the percent difference between TNG SAM and TNG100 predictions for the given property of the selected halo, with yellow and orange points representing agreement within 30%, and magenta and purple points highlighting discrepancies greater than 30%. Although most halos show good agreement across the assessed properties, considerable scatter remains for many halos, particularly for properties such as the SFR and $M_{\rm cold}$, showcasing the limitations of calibrations based on median trends.

was the more appropriate choice for this study given its use in the calibration of the fiducial TNG galaxy formation model and the known resolution-dependent discrepancies in TNG, running this exercise on TNG50 would offer a more comprehensive test of the TNG SAM's ability to reproduce galaxy properties across a wider range of stellar feedback dominated halos. Similarly, running this exercise on the TNG300 simulations would also allow us to investigate the lack of convergence between the different TNG resolutions, potentially uncovering which aspects of the baryon cycle are most sensitive to the varying volumes and resolutions in the simulation suite.

The TNG SAM's focus on replicating the physical processes of galaxy evolution, rather than just the final outcomes, also opens up exciting possibilities for future refinements. Whereas traditional SAMs track mass flows, as we have in this work, Pandya et al. (2023); Carr et al. (2023); Voit et al. (2024a) and Voit et al. (2024b) advocate for the inclusion of explicit tracking of energy flows alongside mass flows. By explicitly tracking the energy budget of the CGM, accounting for both energy sources (e.g., stellar and AGN feedback) and sinks (e.g., radiative cooling and turbulence dissipation), this model enables a more nuanced understanding of the complex interplay of physical processes that shape the CGM and its impact on galaxy evolution.

Integrating such an energy-based CGM model into the TNG SAM would allow for a more self-consistent treatment of feedback processes, where the energy injected by stellar winds and AGN could be directly linked to the thermal and kinetic energy of the CGM. This would provide a more accurate representation of how feedback affects gas cooling, star formation, and other key processes, leading to a more comprehensive and physically motivated picture of galaxy evolution. The strength of this approach lies in its ability to leverage both simulations and observations. The energy-based CGM model can be calibrated against observational constraints on feedback energy and CGM properties at the ISM scale, which are becoming increasingly well-constrained with the advent of high-resolution, multi-wavelength observing facilities (e.g., JWST, MUSE, ALMA). The TNG simulations, in turn, can provide crucial insights into less directly observable aspects, such as the energy budget and dynamics at the CGM scale. This dual calibration, leveraging both simulations and observations, would ensure that the SAM accurately reflects both the theoretical understanding of galaxy evolution and the empirical evidence.

5.3 Comparison to Similar Work

revise using final sam Previous attempts to align the predictions of SAMs with hydrodynamical simulations have varied in methodology, scope, and success. Here, we compare our approach and results with those of Stringer et al. (2010), Neistein et al. (2012) and Mitchell & Schaye (2022), highlighting key differences and similarities, and the relative accuracy of each approach.

Early efforts to reconcile SAMs with hydrodynamic simulations (e.g., Helly et al. (2003), Benson et al. (2001), and Yoshida et al. (2002)) demonstrated that the cooled mass predicted by SAMs and hydrodynamical simulations could be consistent when the SAMs are adapted to emulate the assumptions made by the hydrodynamical simulations. Stringer et al. (2010) expanded this approach by attempting to reproduce the entire formation history of a single disk galaxy within the GASOLINE hydrodynamical simulation using a modified version of the GALFORM SAM. To achieve broad agreement with the simulation data, they adjusted parameters related to gas cooling, star formation, and feedback, demonstrating the potential of SAMs to reproduce the detailed evolution of individual galaxies. However, the focus on a single object left uncertainties about the general applicability of their findings.

Neistein et al. (2012) (hereafter N12) expanded on this to a wider range of galaxies by extracting efficiencies describing accretion, cooling, star formation, and feedback from the OverWhelmingly Large Simulations (OWLS) and applying them within the SAM presented in Neistein & Weinmann (2010) to reproduce OWLS's results. By tuning these efficiencies as functions of halo mass and redshift, they reproduced various global galaxy and halo properties up to $z = 3$ within $\pm 0.1 - 0.2$ dex. In terms of approach and scope, N12 is most similar to our work here with the TNG SAM.

However, there are a range of minor to major differences in our implementations. Similar to the TNG SAM, N12 also applies a halo gas accretion efficiency parameter named $f_a = \frac{\dot{M}^{\rm in}_{\rm CGM}}{\dot{M}_{\rm halo}}$. This term is similar to the TNG SAM's $f_{\rm in,CGM}$, except $f_{\rm in,CGM}$adjusts for the baryon fraction and includes both first-time infall and gas recycling. We both implement this parameter similarly in order to match the rate of gas accretion our respective hydrodynamical simulations. For CGM to ISM cooling, N12 use the inverse cooling time to describe the efficiency of gas cooling, while the TNG SAM explicitly uses the cooling time. check this. Here, our implementation differed significantly. N12 still used the traditional cold mode vs hot mode accretion model, with the efficiency used to scale the rate of cooling from that model. The TNG SAM, however, uses the cooling time to determine the rate of cooling without the "hot mode" vs "cold mode" distinction.

For star formation, N12 tune the star formation efficiency to match OWLS, whereas our TNG SAM scales disk sizes with the virial radius according to the fraction observed in TNG and applies the Kennicutt-Schmidt relation. This approach allows us to replicate the underlying star formation processes in TNG without requiring fixed efficiencies as in N12. Regarding stellar feedback, both N12 and the TNG SAM incorporate efficiency parameters to describe the strength of outflows. However, the TNG SAM includes both galaxy and halo-scale outflows modulated by $\eta_{\rm ISM}$and $\eta_{\rm halo}$, while N12 only accounts for galaxy-scale outflows via $\eta_{\rm ISM}$. Furthermore, the TNG SAM incorporates the outflows in a manner that mirrors TNG's subgrid stellar feedback model, which ties the strength of the outflows to the metallicity of the star-forming gas and the stellar wind velocity. N12 incorporated eta ISM as a simple power law, without additional physical changes. N12 also did not focus on metallicity, completely omitting any metallicity-specific tuning.

Overall, N12 applied less detailed efficiencies to get their SAM to reproduce the OWLS simulation. However, this is because their primary aim was to reproduce the mass of the hot gas, the mass of the cold gas, the stellar mass, and the total mass of the galaxies observed in OWLS. Their approach enabled very good agreement for these quantities, reporting a standard deviation ranging from 0.1 - 0.2 dex for each mass reservoir. However, they reported higher deviations for the SFR, with a standard deviation of 0.5 dex. The TNG SAM, despite aiming to reproduce a wider range of global galaxy and halo properties and extending to higher redshifts ($z = 6$), achieves a comparable within 0.1-0.3 dex for most properties, including the SFR.

More recently, Mitchell & Schaye (2022) (hereafter MS22) built upon the N12 approach to emulate the results of the EAGLE simulations. To achieve agreement with EAGLE, they expanded the N12 model to include efficiencies that describe first-time gas accretion and recycling at the halo scale, as well as galaxy- and halo-scale outflows. Unlike N12, MS22 were primarily interested in reproducing the stellar mass- halo mass relation (SHM) and identifying which parameters in EAGLE were most crucial for accurately predicting the relation, given its use as a fundamental diagnostic for understanding galaxy formation efficiency within a given cosmological model. They found that their updated N12 model reproduced the EAGLE stellar masses to within a few tens of percent, with the largest deviation of ~ 0.25 dex occurring in very low-mass halos, consistent with the accuracy achieved by the TNG SAM for stellar mass.

Moreover, MS22 also demonstrated that the SHM relation in EAGLE is primarily shaped by gas ejection of gas via outflows for halos with $M_{\rm vir}< 10^{12}\ M_\odot$, with halo-scale preventative feedback and recycling of ejected gas playing secondary roles. They also found that the redshift evolution of the SHM relation is most sensitive to the efficiencies of first-time gas accretion and ejection by outflows, and is less sensitive to the efficiency of wind recycling, and of gas consumption by star formation. In the TNG SAM, we find similar trends, with the stellar mass being most sensitive to $\eta_{\rm halo}$, and then $f_{\rm in,CGM}$.

MS22 also investigated how star formation and gas flows affect the relationship between halo mass and the masses of both the ISM and CGM. They found that the CGM mass is most sensitive to variations in gas inflows and outflows, particularly those occurring at the halo scale. This finding is echoed in our analysis of the TNG SAM, where we also observed a strong dependence of the CGM mass in TNG on halo-scale gas flows. However, while MS22 found that the mass of the ISM is more sensitive to halo-scale gas flows compared to stellar mass, the TNG SAM finds that $\eta_{\rm halo}$has comparable impact on $M_{\rm cold}$and $M_{\rm star}$. MS22 found this impact was because the ISM reflects recent accretion, star formation, and outflow activity, while galaxy-scale outflows are more efficient at high redshifts in EAGLE and halo-scale outflows are more efficient at low redshifts. In the TNG SAM, however, the mass of the ISM is directly coupled to the stellar mass through the Kennicutt-Schmidt relation. This implies that any variation in the gas outflow rate, whether originating from the ISM or the CGM, will indirectly affect the stellar mass through its impact on the available gas reservoir for star formation.

A significant difference between the TNG SAM and the above studies is its explicit modeling of metal content and cycling within the hydrodynamical simulation. This step is crucial for incorporating physically motivated TNG-like efficiencies, as many processes in both TNG and EAGLE rely on accurate metallicity predictions. It remains unclear whether the other approaches could replicate metal content as effectively as the TNG SAM. However, given our success using the metal loadings, it is reasonable to assume that incorporating similar metal-tracking mechanisms in those models could yield comparable improvements.

6 SUMMARY AND CONCLUSIONS

In this paper, we introduced the TNG SAM, a recalibrated version of the Santa Cruz semi-analytic model, designed to replicate the complex baryon cycle of galaxies in the IllustrisTNG cosmological hydrodynamical simulations. This model bridges the detailed physical processes captured in hydrodynamical simulations with the computational efficiency of SAMs, offering a powerful tool for studying galaxy evolution. By incorporating TNG's galaxy formation physics into a simplified framework, the TNG SAM allows for deeper insights into the interplay of baryonic processes that shape galaxies.

Focusing on stellar feedback-dominated systems, we aimed to reproduce the baryon cycle in low- to intermediate-mass dwarf galaxies ($M_{\rm halo} \sim 10^{10} - 10^{11}$) and Milky Way-mass galaxies ($M_{\rm halo} \sim 10^{12}$) in TNG100. Using measurements of gas flows from a subset of ~ 400 central galaxies as a proxy for the larger TNG100 sample, we updated the SC SAM's physical prescriptions for halo gas accretion, cooling, stellar feedback, and metal circulation. These updates, implemented as a function of halo mass and redshift, led to more accurate predictions of galaxy-scale properties such as stellar mass, gas content, and metallicity, as well as halo-scale properties like the overall baryon content.

Several key insights about the baryon cycle in TNG emerged from this work, with important implications to keep in mind when building the next generation of SAMs:

(i) *The complexities of gas cooling in TNG necessitate a departure from the traditional "cold mode" vs. "hot mode" dichotomy in SAMs.* In TNG and FIRE, cooling times often exceed dynamical timescales, showing that the simple cold-mode vs. hot-mode framework commonly used in SAMs does not adequately represent the cooling process. The TNG SAM's revised cooling model, calibrated to the cooling times in TNG, results in improved predictions of gas accretion onto galaxies and the mass of the hot halo. This suggests that SAMs need to move beyond the traditional "cold mode" vs. "hot mode" dichotomy and instead adopt models that better reflect the full range of gas cooling timescales seen in hydrodynamical simulations (Section 5.1.2, Figure 11).

(ii) *Global star formation is relatively insensitive to the detailed spatial distribution of gas, but galaxy sizes must be properly calibrated.* Although the TNG SAM applies the Kennicutt-Schmidt relation at the scale of the entire galaxy, while TNG applies it locally, the TNG SAM successfully reproduces the global Kennicutt-Schmidt relation seen in TNG, leading to accurate stellar masses, star formation rates and cold gas masses. This suggests that global star formation rates are relatively insensitive to the spatial distribution of gas within galaxies. However, accurate predictions still require proper calibration of galaxy sizes, which are not adequately captured by the angular momentum models used in SAMs. (Section 5.1.3, Figure 9).

(iii) *Modeling outflows at the galaxy- and halo-scale is essential for accurately predicting the gas content in galaxies.* While galaxy-scale outflows are a well-known driver of galaxy evolution, the TNG SAM highlights that halo-scale outflows are equally critical for accurately predicting gas content. Incorporating TNG's galactic winds model, which ties outflow strength to the metallicity of the cold gas, allowed the TNG SAM to capture not just the behavior of galaxy-scale outflows, but also their continuation into the halo—a channel neglected in most traditional SAMs. This two-step outflow process, where gas flows from the ISM to the CGM and from the CGM to the IGM, provides a more realistic depiction of outflows and avoids the overprediction of hot gas mass and baryon fraction. (Section 5.1.4, Figure 9).

(iv) *Non-uniform metal flows between the ISM and CGM leads to more realistic predictions of galaxy metallicities.* The TNG SAM's use of metallicity-weighted mass-loading factors significantly improves its ability to match the metallicity evolution observed in TNG. This approach compensates for the simplified instantaneous recycling model used in most SAMs, which typically overlook the delayed mixing and transport of metals. By tying feedback strength to gas metallicity, as done in TNG and high-resolution simulations like FIRE and TIGRESS, the TNG SAM demonstrates that future SAMs aiming to adopt more realistic feedback models will need to incorporate metal loadings to properly capture metal cycling processes between the ISM, CGM, and IGM (Section 5.1.5, Figure 9).

ACKNOWLEDGEMENTS

The Acknowledgements section is not numbered. Here you can thank helpful colleagues, acknowledge funding agencies, telescopes and facilities used etc. Try to keep it short.

DATA AVAILABILITY

will make available on github!

REFERENCES

Anderson L. D., Bania T. M., Balser D. S., Cunningham V., Wenger T. V., Johnstone B. M., Armentrout W. P., 2014, The Astrophysical Journal Supplement Series, 212, 1
Behroozi P. S., Wechsler R. H., Wu H.-Y., 2012, The Astrophysical Journal, 762, 109
Benson A. J., 2012, New Astronomy, 17, 175
Benson A. J., Pearce F. R., Frenk C. S., Baugh C. M., Jenkins A., 2001, Monthly Notices of the Royal Astronomical Society, 320, 261
Bernardi M., Meert A., Sheth R. K., Vikram V., Huertas-Company M., Mei S., Shankar F., 2013, Monthly Notices of the Royal Astronomical Society, 436, 697
Bigiel F., Leroy A., Walter F., Brinks E., Blok W. J. G. d., Madore B., Thornley M. D., 2008, The Astronomical Journal, 136, 2846
Boselli A., Cortese L., Boquien M., Boissier S., Catinella B., Lagos C., Saintonge A., 2014, Astronomy & Astrophysics, 564, A66
Bouché N., et al., 2010, The Astrophysical Journal, 718, 1001
Bower R. G., Benson A. J., Crain R. A., 2012, Monthly Notices of the Royal Astronomical Society, 422, 2816
Calette A. R., Avila-Reese V., Rodríguez-Puebla A., Hernández-Toledo H., Papastergis E., 2018, Revista Mexicana de Astronomia y Astrofisica, 54, 443
Carr C., Bryan G. L., Fielding D. B., Pandya V., Somerville R. S., 2023, The Astrophysical Journal, 949, 21
Cattaneo A., et al., 2017, Monthly Notices of the Royal Astronomical Society, 471, 1401
Cole S., 1991, The Astrophysical Journal, 367, 45
Collacchioni F., Cora S. A., Lagos C. D. P., Vega-Martínez C. A., 2018, Monthly Notices of the Royal Astronomical Society, 481, 954
Croton D. J., et al., 2006, Monthly Notices of the Royal Astronomical Society, 365, 11
Croton D. J., et al., 2016, The Astrophysical Journal Supplement Series, 222, 22
Côté B., Silvia D. W., O'Shea B. W., Smith B., Wise J. H., 2018, The Astrophysical Journal, 859, 67
Davis M., Efstathiou G., Frenk C. S., White S. D. M., 1985, The Astrophysical Journal, 292, 371
Davé R., Finlator K., Oppenheimer B. D., 2012, Monthly Notices of the Royal Astronomical Society, 421, 98
Diemer B., et al., 2018, The Astrophysical Journal Supplement Series, 238, 33
Donnari M., et al., 2019, Monthly Notices of the Royal Astronomical Society, 485, 4817
Gabrielpillai A., Somerville R. S., Genel S., Rodriguez-Gomez V., Pandya V., Yung L. Y. A., Hernquist L., 2022, Monthly Notices of the Royal Astronomical Society, 517, 6091
Gallazzi A., Charlot S., Brinchmann J., White S. D. M., Tremonti C. A., 2005, Monthly Notices of the Royal Astronomical Society, 362, 41
Genel S., et al., 2018, Monthly Notices of the Royal Astronomical Society, 474, 3976

Gnedin N. Y., Kravtsov A. V., 2011, The Astrophysical Journal, 728, 88
Guo Q., et al., 2011, Monthly Notices of the Royal Astronomical Society, 413, 101
Guo Q., et al., 2016, Monthly Notices of the Royal Astronomical Society, 461, 3457
Helly J. C., Cole S., Frenk C. S., Baugh C. M., Benson A., Lacey C., Pearce F. R., 2003, Monthly Notices of the Royal Astronomical Society, 338, 913
Henriques B., White S., Thomas P., Angulo R., Guo Q., Lemson G., Springel V., Overzier R., 2015, Monthly Notices of the Royal Astronomical Society, 451, 2663
Hirschmann M., De Lucia G., Fontanot F., 2016, Monthly Notices of the Royal Astronomical Society, 461, 1760
Hopkins P. F., et al., 2018, Monthly Notices of the Royal Astronomical Society, 480, 800
Hopkins P. F., et al., 2023, Monthly Notices of the Royal Astronomical Society, 519, 3154
Karmakar T., Genel S., Somerville R. S., 2023, Monthly Notices of the Royal Astronomical Society, 520, 1630
Kennicutt Jr. R. C., 1998, \apj, 498, 541
Keres D., Yun M. S., Young J. S., 2003, The Astrophysical Journal, 582, 659
Kim C.-G., et al., 2020a, The Astrophysical Journal, 900, 61
Kim C.-G., et al., 2020b, The Astrophysical Journal Letters, 903, L34
Klypin A. A., Trujillo-Gomez S., Primack J., 2011, The Astrophysical Journal, 740, 102
Kravtsov A. V., 2003, The Astrophysical Journal, 590, L1
Kumari N., Irwin M. J., James B. L., 2020, Astronomy & Astrophysics, 634, A24
Lacey C., Silk J., 1991, The Astrophysical Journal, 381, 14
Lacey C. G., et al., 2016, Monthly Notices of the Royal Astronomical Society, 462, 3854
Lagos C. d. P., Lacey C. G., Baugh C. M., 2013, Monthly Notices of the Royal Astronomical Society, 436, 1787
Lagos C. d. P., Tobar R. J., Robotham A. S. G., Obreschkow D., Mitchell P. D., Power C., Elahi P. J., 2018, Monthly Notices of the Royal Astronomical Society, 481, 3573
Li Z.-Y., Nakamura F., 2006, \apj, 640, L187
Lu Y., Kereš D., Katz N., Mo H. J., Fardal M., Weinberg M. D., 2011, Monthly Notices of the Royal Astronomical Society, 416, 660
Marinacci F., et al., 2018, Monthly Notices of the Royal Astronomical Society, 480, 5113
McConnell N. J., Ma C.-P., 2013, The Astrophysical Journal, 764, 184
Mitchell P. D., Schaye J., 2022, Monthly Notices of the Royal Astronomical Society, 511, 2948
Mitchell P. D., et al., 2018, Monthly Notices of the Royal Astronomical Society, 474, 492
Mitchell P. D., Schaye J., Bower R. G., Crain R. A., 2020, Monthly Notices of the Royal Astronomical Society, 494, 3971
Monaco P., Fontanot F., Taffoni G., 2007, Monthly Notices of the Royal Astronomical Society, 375, 1189
Monaco P., Benson A. J., De Lucia G., Fontanot F., Borgani S., Boylan-Kolchin M., 2014, Monthly Notices of the Royal Astronomical Society, 441, 2058
Naiman J. P., et al., 2018, Monthly Notices of the Royal Astronomical Society, 477, 1206
Narayanan D., Krumholz M. R., Ostriker E. C., Hernquist L., 2012, Monthly Notices of the Royal Astronomical Society, 421, 3127
Navarro J. F., Frenk C. S., White S. D. M., 1996, The Astrophysical Journal, 462, 563
Neistein E., Weinmann S. M., 2010, Monthly Notices of the Royal Astronomical Society, 405, 2717
Neistein E., Khochfar S., Dalla Vecchia C., Schaye J., 2012, Monthly Notices of the Royal Astronomical Society, 421, 3579
Nelson D., et al., 2018, Monthly Notices of the Royal Astronomical Society, 475, 624
Nelson D., et al., 2019, Monthly Notices of the Royal Astronomical Society, 490, 3234
Obreschkow D., Croton D., Lucia G. D., Khochfar S., Rawlings S., 2009, The Astrophysical Journal, 698, 1467
Okamoto T., Gao L., Theuns T., 2008, Monthly Notices of the Royal Astronomical Society, 390, 920
Pakmor R., Springel V., 2013, Monthly Notices of the Royal Astronomical Society, 432, 176
Pakmor R., Bauer A., Springel V., 2011, Monthly Notices of the Royal Astronomical Society, 418, 1392
Pandya V., 2021, PhD thesis, UC Santa Cruz, `https://escholarship.org/uc/item/9xc1v7c9`
Pandya V., et al., 2020, The Astrophysical Journal, 905, 4
Pandya V., et al., 2021, Monthly Notices of the Royal Astronomical Society, 508, 2979
Pandya V., et al., 2023, The Astrophysical Journal, 956, 118
Peeples M. S., Shankar F., 2011, Monthly Notices of the Royal Astronomical Society, 417, 2962
Peeples M. S., Werk J. K., Tumlinson J., Oppenheimer B. D., Prochaska J. X., Katz N., Weinberg D. H., 2014, The Astrophysical Journal, 786, 54
Pillepich A., et al., 2018a, Monthly Notices of the Royal Astronomical Society, 473, 4077
Pillepich A., et al., 2018b, Monthly Notices of the Royal Astronomical Society, 475, 648
Pillepich A., et al., 2019, Monthly Notices of the Royal Astronomical Society, 490, 3196
Planck Collaboration et al., 2016, Astronomy & Astrophysics, 594, A13
Popping G., Somerville R. S., Trager S. C., 2014, Monthly Notices of the Royal Astronomical Society, 442, 2398
Popping G., et al., 2019, The Astrophysical Journal, 882, 137
Porter L. A., Somerville R. S., Primack J. R., Johansson P. H., 2014, Monthly Notices of the Royal Astronomical Society, 444, 942
Rodriguez-Gomez V., et al., 2015, Monthly Notices of the Royal Astronomical Society, 449, 49
Rodríguez-Puebla A., Primack J. R., Avila-Reese V., Faber S. M., 2017, Monthly Notices of the Royal Astronomical Society, 470, 651
Saro A., De Lucia G., Borgani S., Dolag K., 2010, Monthly Notices of the Royal Astronomical Society, 406, 729
Somerville R. S., Davé R., 2015, Annual Review of Astronomy and Astrophysics, 53, 51
Somerville R. S., Primack J. R., 1999, Monthly Notices of the Royal Astronomical Society, 310, 1087
Somerville R. S., Hopkins P. F., Cox T. J., Robertson B. E., Hernquist L., 2008a, Monthly Notices of the Royal Astronomical Society, 391, 481
Somerville R. S., et al., 2008b, The Astrophysical Journal, 672, 776
Somerville R. S., Gilmore R. C., Primack J. R., Domínguez A., 2012, Monthly Notices of the Royal Astronomical Society, 423, 1992
Somerville R. S., Popping G., Trager S. C., 2015, Monthly Notices of the Royal Astronomical Society, 453, 4337
Springel V., 2010, Monthly Notices of the Royal Astronomical Society, 401, 791
Springel V., Hernquist L., 2003, Monthly Notices of the Royal Astronomical Society, 339, 289
Springel V., White S. D. M., Tormen G., Kauffmann G., 2001, Monthly Notices of the Royal Astronomical Society, 328, 726
Springel V., et al., 2018, Monthly Notices of the Royal Astronomical Society, 475, 676
Stringer M. J., Brooks A. M., Benson A. J., Governato F., 2010, Monthly Notices of the Royal Astronomical Society, 407, 632
Sutherland R. S., Dopita M. A., 1993, The Astrophysical Journal Supplement Series, 88, 253
Torrey P., Vogelsberger M., Genel S., Sijacki D., Springel V., Hernquist L., 2014, Monthly Notices of the Royal Astronomical Society, 438, 1985
Vogelsberger M., Genel S., Sijacki D., Torrey P., Springel V., Hernquist L., 2013, Monthly Notices of the Royal Astronomical Society, 436, 3031
Voit G. M., Pandya V., Fielding D. B., Bryan G. L., Carr C., Donahue M., Oppenheimer B. D., Somerville R. S., 2024a, Equilibrium States of Galactic Atmospheres I: The Flip Side of Mass Loading, doi:10.48550/arXiv.2406.07631, `http://arxiv.org/abs/2406.07631`
Voit G. M., Carr C., Fielding D. B., Pandya V., Bryan G. L., Don-

ahue M., Oppenheimer B. D., Somerville R. S., 2024b, Equilibrium States of Galactic Atmospheres II: Interpretation and Implications, doi:10.48550/arXiv.2406.07632, http://arxiv.org/abs/2406.07632
Weinberger R., et al., 2017, Monthly Notices of the Royal Astronomical Society, 465, 3291
White S. D. M., Frenk C. S., 1991, The Astrophysical Journal, 379, 52
White S. D. M., Rees M. J., 1978, Monthly Notices of the Royal Astronomical Society, 183, 341
Wise J. H., Turk M. J., Norman M. L., Abel T., 2011, The Astrophysical Journal, 745, 50
Wright R. J., Lagos C. d. P., Power C., Mitchell P. D., 2020, Monthly Notices of the Royal Astronomical Society, 498, 1668
Wright R. J., Somerville R. S., Lagos C. d. P., Schaller M., Davé R., Anglés-Alcázar D., Genel S., 2024, The baryon cycle in modern cosmological hydrodynamical simulations, doi:10.48550/arXiv.2402.08408, http://arxiv.org/abs/2402.08408
Yoshida N., Stoehr F., Springel V., White S. D. M., 2002, Monthly Notices of the Royal Astronomical Society, 335, 762
Yung L. Y. A., Somerville R. S., Finkelstein S. L., Popping G., Davé R., 2019, Monthly Notices of the Royal Astronomical Society, 483, 2983
Yung L. Y. A., et al., 2023, Monthly Notices of the Royal Astronomical Society, 519, 1578
Zahid H. J., Geller M. J., Kewley L. J., Hwang H. S., Fabricant D. G., Kurtz M. J., 2013, The Astrophysical Journal Letters, 771, L19

APPENDIX A: ANALYTIC SCALING RELATIONS FOR THE TNG SAM

We alternatively calibrated the SC SAM using analytic scaling relations as a function of halo mass and redshift using the following sophisticated functional form:

$$\log(f(M_{\rm halo}, z, b, c, d, \alpha_0, \alpha_z)) = \\ -a(\arctan(b \cdot [\log(M_{\rm halo}) - c]) + d) \cdot [\alpha_0 + e^{\alpha_z}(1+z)] \qquad \text{(A1)}$$

Using these scaling relations also provided agreements with TNG within the same range as the linearly interpolated values. All coefficients used in Equation A1 are described in Table A1.

APPENDIX B: MODIFICATIONS TO THE SC SAM PRESENTED

The modifications described in Section **??** had the most substantial impact on the halo-scale properties of the Santa Cruz SAM. The updated cooling model significantly improved the prediction of the hot halo gas mass, previously underestimated by several orders of magnitude, as shown in Figure **??** and first noted in Pandya et al. (2020). Naturally, this correction also led to a substantial improvement in the SAM's prediction of the baryon fraction, illustrated in the lower panel of Figure **??**. Although these changes drastically affected the halo-scale gas properties, the impact on the ISM-scale gas properties and overall metal content was minimal, with deviations from the original Santa Cruz SAM reaching a maximum of 0.5 dex.

$$\epsilon_{\rm halo} = (\eta_{\rm halo} + \eta_{\rm ISM}) V_{\rm vir}^2 / V_{\rm SN}^2 \qquad \text{(B1)}$$

here, $V_{\rm SN}$ = 630 km/s is a constant.

This paper has been typeset from a TEX/LATEX file prepared by the author.

Model Update	Parameter	Description	Coefficients (a, b, c, d, α_0, α_z)/ Value	Comments
Gas Cooling	$f_{\mathrm{in,CGM}}$		1.15, 0.0088, 10.2189, 0.0454, -3.5025, -1.0791	
...	t_{cool}		1.15, 9.4401, 11.5681, 359.5587, -0.0275, -7.4258	
Star Formation	$R_{\mathrm{disk,TNG}}/R_{\mathrm{disk,SAM}}$		1.0, 0.0009, 9.4550, -0.0028, 9.2402, 4.2137	
Stellar Feedback	$\eta_{\mathrm{launch}}/\eta_{ISM}$		1.2, 6.7252, 11.6654, 4.6427, -0.1362, -3.7849	
...	η_{halo}		0.85, -1.6941, 10.8106, 1.7008, -0.7913, -3.1102	
Metal Circulation	$\zeta_{\mathrm{in,halo}}$		1.0, -5.0310, 11.3533, 7.8483, 0.1622, -4.3837	
...	$\zeta_{\mathrm{out,halo}}$		1.0, 4.0473, 11.3201, -0.0693, -0.1187, -2.9203	
...	$\zeta_{\mathrm{in,ISM}}$		1.0, 1.1155, 10.0801, -1.4657, 0.0161, -2.9189	
...	$\zeta_{\mathrm{out,ISM}}$		1.0, 48.4092, -62.9615, 5.9549, 0.0501, -18.1282	$z <= 1$
...	...		1.0, 7.6844, 13.7629, 1.4179, -4.2491, -0.8384	$z > 1$

Table A1. Parameters calibrated to match TNG and the coefficients used in Equation A1. (1) Parameter; (2) SAM Label; (3) TNG Label; (4) comment.

Scale	Parameter	SAM Label	TNG Label	Description
Halo	M_{halo}	`GalpropMvir`	`Group_M_TopHat_200['SubhaloGrNr']`	Total virial mass
	M_{DM}	`GalpropMvir` $(1 - f_{\mathrm{baryon}})$	`SubhaloMassType Part 1 (DM)`	Total dark matter mass
	M_{CGM}	`HalopropMhot`	`GroupMassType part 0 ['SubhaloGrNr']`	Gas mass of the circumgalactic halo
Galaxy	M_*	`GalpropMstar`	`SubhaloMassInRadType part 4`	Stellar mass
	M_{ISM}	`GalpropMcold`	`SubhaloMassInRadType part 0`	Gas mass of the interstellar medium
	SFR	`GalpropSfr`	`SubhaloSFR`	Star formation rate
	R_{disk}	`GalpropRdisk`	$2 \cdot$ `SubhaloHalfmassRadType part 4`	Twice stellar half mass radius
	Z_*	`GalpropZstar`	`SubhaloStarMetallicity`	Stellar metallicity
	Z_{ISM}	`GalpropZcold`	`SubhaloGasMetallicitySfr`	ISM gas metallicity
	Z_{CGM}	`HalopropZhot`	`GroupGasMetallicity['SubhaloGrNr']`	Halo gas metallicity

Table A2. Correspondence between the parameters studied in this paper, their fields in the SAM, and their corresponding fields in the IllustrisTNG simulations. A description of each parameter is also provided.

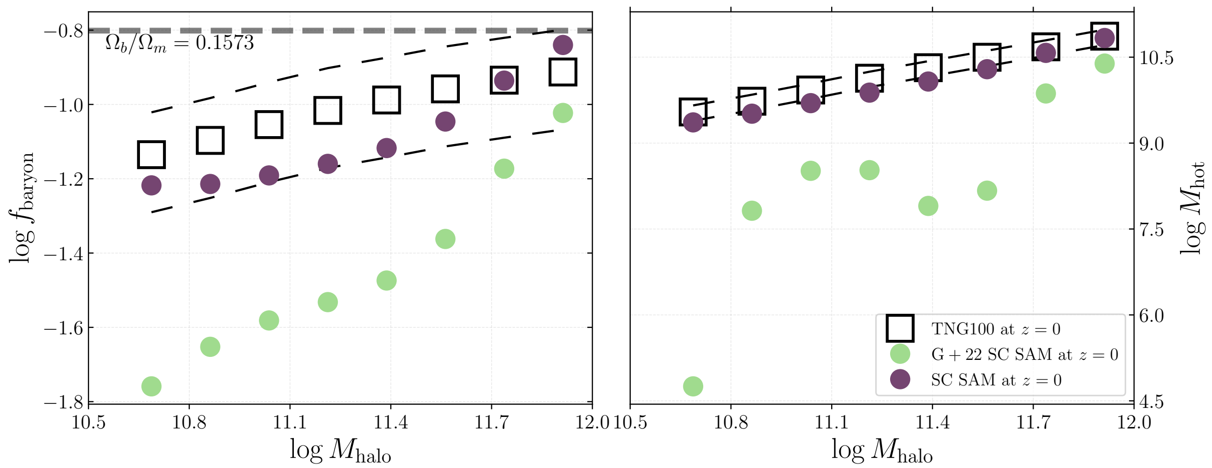

Figure B1. old updating